University of Reading

Global mean sea level over the past 4.5 million years

Article

Accepted Version

Clark, P. U., Shakun, J. D., Rosenthal, Y., Pollard, D., Hostetler, S. W., Köhler, P., Bartlein, P. J., Gregory, J. M., Zhu, C., Schrag, D. P., Liu, Z. and Pisias, N. G. (2025) Global mean sea level over the past 4.5 million years. Science, 390 (6770). eadv8389. ISSN 1095-9203 doi: 10.1126/science.adv8389 Available at https://centaur.reading.ac.uk/125301/

It is advisable to refer to the publisher's version if you intend to cite from the work. See Guidance on citing.

To link to this article DOI: http://dx.doi.org/10.1126/science.adv8389

Publisher: American Association for the Advancement of Science

All outputs in CentAUR are protected by Intellectual Property Rights law, including copyright law. Copyright and IPR is retained by the creators or other copyright holders. Terms and conditions for use of this material are defined in the End User Agreement.

www.reading.ac.uk/centaur

CentAUR

University of Reading

Central Archive at the University of Reading

Reading's research outputs online

Global sea level over the past 4.5 million years

Peter U. Clark[1,2,†], Jeremy D. Shakun[3,†], Yair Rosenthal[4,5], David Pollard[6], Steven W. Hostetler[1], Peter Köhler[7], Patrick J. Bartlein[8], Jonathan M. Gregory[9,10], Chenyu Zhu[11], Daniel P. Schrag[12], Zhengyu Liu[13], Nicklas G. Pisias[1]

[1]College of Earth, Ocean, and Atmospheric Sciences, Oregon State University, Corvallis, OR 97331
[2]School of Geography and Environmental Sciences, University of Ulster, Coleraine, Northern Ireland, UK BT52 1SA
[3]Department of Earth and Environmental Sciences, Boston College, Chestnut Hill, MA 02467
[4]Department of Marine and Coastal Science, Rutgers The State University, New Brunswick, NJ 08901
[5]Department of Earth and Planetary Sciences, Rutgers The State University, New Brunswick, NJ 08901
[6]Earth and Environmental Systems Institute, Pennsylvania State University, University Park, PA 16802
[7]Alfred-Wegener-Institut Helmholtz-Zentrum für Polar- und Meeresforschung, Bremerhaven, Germany
[8]Department of Geography, University of Oregon, Eugene, OR 97403-1251
[9]National Center for Atmospheric Science, University of Reading, Reading, UK
[10]Met Office Hadley Centre, Exeter, UK
[11]Institute of Atmospheric Physics, Chinese Academy of Sciences, Beijing, China
[12]Department of Earth and Planetary Sciences, Harvard University, Cambridge, MA 02138
[13]Department of Geography, The Ohio State University, Columbus, OH 43210

[*]Correspondence to: clarkp@onid.orst.edu
†These authors contributed equally to this work.

Abstract

The history of global mean sea level (GMSL) during the late Cenozoic remains uncertain. Here we use a new reconstruction of changes in $\delta^{18}O$ of seawater to reconstruct GMSL over the past 4.5 million years that accounts for temperature-driven changes in the $\delta^{18}O$ of the main ice sheets. Between 4.5 and 3 million years ago (Ma), sea-level highstands remained up to 20 m above present while the first lowstands below present suggest onset of Northern Hemisphere (NH) glaciation at 4 Ma. Intensification of NH glaciation occurred from 3 Ma to 2.5 Ma, culminating in lowstands that were comparable to or lower than the Last Glacial Maximum lowstand 21 ka and that reoccurred throughout much of the Pleistocene. We attribute the middle Pleistocene transition in ice-sheet variability to modulation of 41-kyr obliquity forcing by an increase in ~100-kyr CO_2 variability.

The record of $\delta^{18}O$ measured in benthic foraminifera shells ($\delta^{18}O_b$) (Fig. 1A) is widely used to represent the long-term evolution of combined changes in ocean temperature and global mean sea level (GMSL) over the Cenozoic (*1-5*) as well as to evaluate the response of the climate system to forcings on orbital and tectonic timescales (10^4-10^6 yr) (*6-9*). The fidelity of this record as a global signal has improved with the stacking of multiple records that increases the signal-to-noise ratio (*10-12*) and the use of several independent dating methods that provide a robust chronology (*1, 11, 13, 14*). Different strategies have then been used to decompose the $\delta^{18}O_b$ record into its temperature ($\delta^{18}O_T$) and seawater ($\delta^{18}O_{sw}$) components, with the former reflecting the temperature that the benthic foraminifera shells formed in (larger $\delta^{18}O_T$ in lower temperature) and the latter largely reflecting global ice volume (larger $\delta^{18}O_{sw}$ when more land ice). Although these strategies share the same goal, their different underlying assumptions have resulted in solutions with pronounced differences during the late Pliocene, early Pleistocene (beginning 2.6 Ma), and the middle Pleistocene transition (MPT) (1.5-0.9 Ma) (fig. S1), thus confounding understanding of these critical periods of late-Cenozoic climate and GMSL change.

We address these issues by reconstructing GMSL for the past 4.5 million years (Myr) that circumvents several shortcomings associated with previous reconstructions (see supporting information, section 1). Using our new reconstruction of changes in global mean ocean temperature (ΔMOT), we previously decomposed a $\delta^{18}O_b$ stack (*12*) that includes a correction for possible diagenesis (*15, 16*) and the carbonate-ion effect on foraminifera (*17*) into its $\delta^{18}O_T$ and $\delta^{18}O_{sw}$ components (*18*). Here we convert our $\delta^{18}O_{sw}$ reconstruction (fig. S2C) to GMSL by applying a mass-balance approach that conserves $\delta^{18}O$ changes of the global ocean and the North American (Laurentide and Cordilleran) (NAIS), Eurasian (EUR), Greenland (GRN), and Antarctic (ANT) ice sheets, including loss of marine-based ANT ice (*19, 20*) (see the supplementary

materials, section 2). In doing so, our model accounts for time-varying temperature (*21*) and ice-volume effects on the $\delta^{18}O$ of ice sheets ($\delta^{18}O_i$) over the past 4.5 Myr that yields a variable relationship between $\delta^{18}O_{sw}$ and sea level (fig. S3), as opposed to methods that convert $\delta^{18}O_{sw}$ to sea level using a constant linear scaling between $\delta^{18}O_{sw}$ and sea level (*22-26*) or a variable scaling developed for just the last glacial cycle (*27, 28*).

Global mean sea level over the past 4.5 Myr

Our new reconstruction (Fig. 1C) shows that GMSL was largely above present from 4.5-4.0 Ma, with sea-level highstands of ~20 m and sea-level fluctuations of 5-20 m suggesting contributions likely from some combination of changes in GRN and ANT ice sheets although contributions from NAIS or EUR ice sheets cannot be excluded. Subsequent highstands between 4 and 3 Ma remained 15-20 m above present but lowstands now began to extend regularly below present by as much as -50 to -80 m thus marking the onset of extensive NH (NAIS, EUR) glaciation at ~4 Ma. The intensification of NH glaciation from 3 Ma to 2.5 Ma was marked by highstands that decreased to near-modern levels and lowstands that progressively decreased from -55±29 m at 3 Ma to -151±25 m at 2.52 Ma, which is comparable to or lower than the Last Glacial Maximum (LGM, 21 ka) lowstand (-132±15 m) (Fig. 1C). Since 2.5 Ma, sea-level highstands have been within +10 m of present except between 2.25 Ma to 1.45 Ma when they remained as much as 50 m below present, suggesting incomplete deglaciation of NH ice sheets, while fluctuations of large LGM-size ice sheets continued throughout the Pleistocene.

Three factors used to derive our GMSL reconstruction combine to indicate that early Pleistocene ice sheets were comparable in size to the LGM in contrast to several previous reconstructions that suggest that such large ice sheets did not appear until after the MPT (fig. S6A-D). First, with a ΔMOT that is ~50% of a corresponding change in global mean sea surface

89 temperature (ΔSST) before the MPT (*18*), the increasing (cooling) trend of $\delta^{18}O_T$ is smaller in our
90 reconstruction than if ΔMOT:ΔSST=1 is assumed throughout the Pleistocene. Being a residual
91 from the observed $\delta^{18}O_b$, our $\delta^{18}O_{sw}$ is thus more negative during the Pliocene and has a larger
92 increasing trend between 3.0-2.5 Ma (compare figs. S2A and S2B). Second, because ΔMOT:ΔSST
93 was smaller during the early Pleistocene, so was glacial-interglacial MOT variability (*15*), limiting
94 the contribution of $\delta^{18}O_T$ to glacial cycles in $\delta^{18}O_b$, in contrast to the middle and late Pleistocene
95 when ocean temperature and ice volume exerted similar-size controls on $\delta^{18}O_b$. Third, we find that
96 higher global mean surface temperature (GMST) during the early Pleistocene caused the ice sheets
97 to be isotopically heavier (fig. S3D). This reduced their influence on $\delta^{18}O_{sw}$ relative to the
98 isotopically lighter ice sheets during the middle and late Pleistocene. At the same time, given our
99 reconstructed $\delta^{18}O_T$, Ref. (*18*) identified the need to remove a spurious increasing trend from the
100 $\delta^{18}O_b$ stack attributed to diagenesis (*15, 16*) or the carbonate-ion effect on benthic foraminifera
101 (*17*) that, if unaccounted for, would have resulted in even more positive Pliocene $\delta^{18}O_{sw}$ values
102 and larger early Pleistocene ice volumes than in our reconstruction (compare figs. S2B and S2C
103 and figs. S2E and S2F).

104 The spectral characteristics of our GMSL reconstruction are dominated by 41-kyr variance
105 until ~1.2 Ma, followed by the emergence of a ~100-kyr signal during the MPT with similar
106 concentrations of ~100-kyr and 41-kyr variance and a small concentration of 23-kyr variance over
107 the past 0.8 Myr with (Fig. 2A, 2B). A 41-kyr filtered sea-level signal displays long-term (1 Myr)
108 amplitude modulation of obliquity forcing until ~1 Ma, with lowest coherence between both
109 occurring during intervals of lower amplitude variations (i.e., nodes) (Fig. 2C, 2D). The increase
110 in amplitude after the first node centered on 3.3-3.1 Ma may reflect a threshold response to the
111 increase in obliquity forcing that led to the intensification of NH glaciation (*29*). The below-present

112 highstands and reduced variability between 2.25 Ma and 1.45 Ma (Fig. 1F) are associated with the
113 second node at ~1.8 Ma (Fig. 2C, 2D). The decrease in amplitude after the third node ~1 Ma
114 reflects the decrease in size of 41-kyr ice sheets relative to those that characterized the Pleistocene
115 prior to 1 Ma, with large ice sheets now occurring less frequently (every ~100 kyr) (Fig. 1C).

116 The evolution of changes in sea-level variability over the past 2.5 Myr as measured by sea-
117 level terminations (defined as the maximum rate of sea-level rise during deglaciations) (Fig. 3D)
118 shares the same relationship to obliquity as similarly defined GMST terminations (Figure 3B).
119 This includes the occurrence of terminations between 2.5 Ma and 1.2 Ma for every (near-)
120 maximum in obliquity, as previously found with an independent age model (*13*), except during the
121 node in obliquity modulation centered on 1.8 Ma (Fig. 2C, 2D) when a small concentration of
122 precessional variance appears (Figure 3F).

123 Over the past 1.2 Myr, we identify eight intervals (M8-M1) that begin and end with sea-
124 level terminations associated with rising or peak obliquity (Fig. 3), with good agreement (within
125 0.5-4 kyr) between the mean ages of terminations during the past 1 Myr derived here and those
126 derived from radiometric dating (*14, 30, 31*). Each of the eight intervals brackets 1-2 obliquity
127 peaks without a corresponding termination (Fig. 3D, 3E), consistent with previous work (*13, 32,*
128 *33*). This low-frequency signal first appears 1.19 Ma during the 72-kyr M8 interval. This pattern
129 is repeated for the 78-kyr M7 interval between Terminations X (0.87 Ma) and IX (0.79 Ma) and
130 the 89-kyr M6 interval between Terminations VIII (0.71 Ma) and VII (0.62 Ma), with each of these
131 two intervals followed by a shorter length interval when a termination accompanies an obliquity
132 maximum. A similar interval of one skipped obliquity cycle between Terminations X and XII was
133 inferred from a $\delta^{18}O_b$ record (*14*) but our ΔGMST and GMSL reconstructions show that the
134 intervening Termination XI was as large as some earlier terminations (Fig. 3B, 3D). Five more

intervals with 1-2 skipped obliquity cycles (M5-M1) span all of the past 0.53 Myr except for one brief 29-kyr interval between M3 and M2 (*31*) which reflects a temperature and sea-level oscillation during Marine Isotope Stage 7 associated with the strongest obliquity forcing since 2.5 Ma (Fig. 3C). The average duration of the M7-M1 intervals is 93.9±13.4 kyr, resulting in the "100-kyr cycle" seen in the late-Pleistocene spectra of ΔGMST and GMSL (Fig. 3F) and their rates of change (Figs. 3B, 3D). One notable difference is that GMSL terminations throughout the Pleistocene only occur after sea level falls below -80 m followed by the next increase to (near-) obliquity maxima (Fig. 3E), suggesting that ice sheets become unstable when exceeding this size, whereas GMST terminations have no comparable temperature threshold.

Our reconstruction of Pliocene highstands and the onset of NH glaciation between 4 and 3 Ma is in good agreement with other studies (*34-36*) including one that subtracted local temperature from $\delta^{18}O_b$ to derive $\delta^{18}O_{sw}$ and sea level as done here (*37*) (fig. S5). A similar local temperature-based reconstruction reproduces the intensification of NH glaciation that culminated in a LGM-like sea-level lowstand at ~2.5 Ma (*26*) (fig. S5) while another reproduces large ice sheets throughout the Pleistocene (*38*) (fig. S6E). To first order, the similarity between temperature-based sea-level reconstructions and our GMSL reconstruction is due to the local temperature reconstructions being nearly the same as our ΔMOT reconstruction (*18*). Several additional lines of evidence identify early Pleistocene NH ice sheets that were at or beyond their LGM extents by ~2.5 Ma, including well-dated terrestrial (*39, 40*), marine (*41, 42*), and geophysical (*43*) records (Fig. 1D) and ice-rafted debris records in the North Atlantic (*44*) and North Pacific (*45*) oceans (Fig. 1E), consistent with them being volumetrically as large as at the LGM.

In contrast, changes in Pleistocene GMSL inferred from the $\delta^{18}O_b$ record (*46, 47*) (Fig. 1A) and from several reconstructions derived from it (*9, 22, 25, 27, 28*) find that the culminating

158 lowstand at 2.5 Ma was only ~40% that of the LGM lowstand. Subsequent lowstands then
159 remained at a similar intermediate level (~ -50 m) until the MPT when they furthered lowered,
160 reaching LGM-like levels by 0.8 Ma (fig. S6A-D). Given the robust evidence for spatially
161 extensive early Pleistocene ice sheets (Fig. 1D, 1E), the associated intermediate-size lowstands
162 imply low-aspect ratio ice sheets relative to those following the MPT (i.e., on average thinner,
163 since the ice volume is less but the area the same). This was the basis for the regolith hypothesis
164 for the MPT (*48*). We attribute these findings of intermediate-size early Pleistocene ice sheets to
165 the underlying methods that, by default, preserve the variability of the $\delta^{18}O_b$ record, including the
166 increase in the size of glaciations during the MPT, with a further underestimation of early
167 Pleistocene glaciations due to the lack of accounting for the long-term decrease in GMST on $\delta^{18}O_i$
168 (Fig. S3) (see the supplementary materials, section 1). Lastly, the good agreement between our
169 reconstruction and all those that cover the past 0.8 Myr (fig. S7) suggest a robust understanding of
170 GMSL since the MPT.

171 **Towards resolving the paradox of large early Pleistocene ice sheets**

172 A well-known paradox posed by early Pleistocene GMSL reconstructions is that their
173 spectra are dominated by 41-kyr variability despite peak summer insolation being dominated by
174 precession (*49*). Coupled climate and ice-sheet models have reproduced NH ice-sheet 41-kyr
175 variability when accounting for albedo feedbacks, the integrated summer insolation forcing, and
176 thin ice sheets with ablation zones that remained poleward of 60°N (*33, 50, 51*). However, such
177 ice sheets are inconsistent with the geologic evidence for their southern margins in North America
178 reaching 39°N during the early Pleistocene (Fig. 1D) (*39, 52*) and they would not dominate the
179 variability seen in our reconstruction. Another hypothesis proposes that higher early Pleistocene
180 temperatures caused the response of the ANT ice sheet to precessional forcing to be out of phase

with NH ice sheets, thus cancelling the 23-kyr signal in sea-level records (*53*). However, hemispheric ΔSST reconstructions show a dominant in-phase 41-kyr signal with virtually no precessional power (*21*) and this hypothesis cannot account for the large obliquity-driven NH ice sheets in our reconstruction which had about twice the volume as modeled by Ref. (*53*).

We propose that obliquity forced variations in the Southern Ocean carbon cycle during the early Pleistocene caused dominant $[CO_2]_{atm}$ variability at this frequency (*54*). At the same time, the dominant 41-kyr signal of Southern Ocean SSTs and the temperature effects of related changes in the position of the sea-ice edge would have been advected through the shallow meridional circulation and upwelled in the equatorial Pacific (*55, 56*), where they combined with the SST variability from CO_2 forcing to induce the observed dominant 41-kyr SST signal at these low latitudes (*21, 57*). Observations (*58*) and modeling (*59*) show that changes in equatorial Pacific SSTs can strongly influence NH ice-sheet surface mass balance (SMB), with the ice-sheet changes then potentially acting as a positive feedback on equatorial Pacific SSTs (*60*).

Our results pose another dimension to this paradox in showing that large ice sheets existed throughout the Pleistocene while glacial GMSTs underwent a ~6ºC long-term cooling (Figs. 1B, 1C), with polar amplification causing an even greater amount of cooling experienced by the high-latitude ice sheets (*21*). This relationship is further complicated by the strong effect that ice sheets have on their own local climate (*61*). We propose that the effects of higher early Pleistocene temperatures on ice-sheet SMB were mitigated by an associated increase in high-latitude precipitation directly from warming (Clausius-Clapeyron relationship) as well as from latitudinal shifts in the westerlies as SST gradients changed (*62*). We can then infer that while cooling decreased accumulation over glaciated regions, the same cooling reduced surface ablation and thus caused SMB to remain positive. Similar transient relationships between other factors affecting

SMB such as the influence of clouds on ice-sheet surface energy balance (*63, 64*) or terrestrial ecosystem emissions and atmospheric chemistry (*65*) can also be considered. If involved, changes in these transient feedbacks with global cooling continued to combine in such a way as to induce ice-sheet SMB that supported the growth of large ice sheets and then maintained their presence in response to obliquity forcing, suggesting an extraordinary balancing act that allowed the inception and growth of ice sheets to their maximum size under a range of GMST and $[CO_2]_{atm}$.

To explore this issue further, we conducted several experiments with the GENESIS V3.0 climate model (*66, 67*) to examine the sensitivity of early Pleistocene NH ice-sheet SMB to orbits, atmospheric CO_2, and ice-sheet height (see supporting information, section 4, Table S1). We first assessed our modeling strategy by running an experiment with LGM boundary conditions and found that the simulated NH ice sheets are in or have positive SMB. Our sensitivity experiments for early Pleistocene ice sheets included various combinations of orbits corresponding to low (at 2.165 Ma) and high (at 2.145 Ma) obliquity (*68*), $[CO_2]_{atm}$ of 200 and 300 ppmv that covers much of the range suggested by proxies (*69*), and three ice-sheet configurations that assess sensitivity to ice-sheet height for a given LGM area (Table S1). Our results suggest that early Pleistocene ice sheets that were larger than LGM ice sheets could have been in SMB with low obliquity and $[CO_2]_{atm}$ of 300 ppmv. SMB becomes more negative as ice-sheet height is lowered to LGM values unless there is a compensatory decrease in $[CO_2]_{atm}$. No decrease in $[CO_2]_{atm}$ within the range of our current understanding of its Pleistocene variability could support the low-aspect-ratio ice sheets in SMB inferred by the regolith hypothesis (*48*).

We thus conclude that the extra height of the early Pleistocene ice sheets relative to the LGM was critical to them being in SMB during glaciations. Given our finding that the large ice sheets shared a common size threshold throughout the Pleistocene equivalent to sea level below -

80 m that, when exceeded, triggered ice-sheet instabilities that culminated in a termination (Fig. 3E), we have narrowed this aspect of the paradox to understanding how different boundary conditions and feedbacks may have contributed to the inception and growth of the early Pleistocene ice sheets.

Towards resolving the paradox of the middle Pleistocene transition and the origin of the ~100-kyr cycle

The longstanding MPT paradox relates to the increase in amplitude and decrease in frequency of GMSL variability during the MPT in the absence of any corresponding change in orbital forcing (*4*). Our finding that large ice sheets existed throughout the Pleistocene, however, challenges several key aspects of their behavior that are usually invoked to explain this paradox: (i) that large ice sheets developed during the MPT in response to long-term changes internal to the climate system (*4, 48, 70-75*), (ii) that the time constant for growth of large ice sheets is significantly longer than for ice-sheet decay, giving rise to ~100-kyr cycles (*76-78*), and (iii) that through their large inertia and influence on climate, the large ice sheets drove the ~100-kyr cycle in the rest of the climate system (*8, 79, 80*).

We first note that because pre-MPT ice sheets were as large as those after the MPT, their albedo forcing should have remained largely the same throughout the Pleistocene and thus cannot explain the large increase in orbital-scale GMST variability during the MPT (Fig. 1B). Instead, we attribute that increase to an increase in CO_2 variability associated with changes in the Southern Ocean carbon cycle. Ref. (*21*) proposed that the gradual cooling of the Southern Ocean through the early Pleistocene initiated the MPT in GMST at ~1.5 Ma when average extratropical Southern Hemisphere SSTs first decreased below pre-industrial, increasing the sensitivity of sea ice to the dominant obliquity forcing at these high latitudes. Increased cooling of the Southern Hemisphere

250 also led to an equatorward shift of the westerly winds (*81*), an increase in dust flux to the Southern
251 Ocean (*82*), and greater stratification of surface waters (*83*). Through their impacts on the Southern
252 Ocean carbon cycle (*81, 82, 84-87*), these changes increased carbon storage during glaciations,
253 thus increasing obliquity-scale variability of $[CO_2]_{atm}$ and GMST. However, a further decrease and
254 then stabilization of Southern Ocean ΔSSTs at the end of the MPT ~0.9 Ma then muted the
255 response of the Southern Ocean carbon cycle to obliquity forcing that may have dominated
256 $[CO_2]_{atm}$ variability during the early Pleistocene, with an attendant large decrease in the
257 concentration of 41-kyr variance in $[CO_2]_{atm}$ and GMST (*21*).

258 We similarly attribute the decrease in large-ice-sheet 41-kyr variance across the MPT (Fig.
259 2A, 2B) to modulation of obliquity forcing by the newly established decrease in $[CO_2]_{atm}$ and
260 GMST variance. Specifically, prior to reaching their maximum size at the end of each of the M
261 intervals, ice-sheet response to low obliquity was modulated by periods of higher $[CO_2]_{atm}$ and
262 GMST, and vice versa, with times of maximum ice-sheet growth only occurring when the next
263 obliquity low combined with low $[CO_2]_{atm}$ and GMST (Figs. 4A, 4B, 4C). The initial retreat of
264 large ice sheets in response to the next increase in obliquity then triggered a sequence of events
265 and feedbacks leading to a termination every ~100 kyr (*31*). Among these feedbacks are large-ice-
266 sheet instabilities that sustained ice-sheet retreat (*8, 77, 88-91*) which, through its influence on the
267 Atlantic meridional overturning circulation, induced warming of the Southern Ocean with an
268 associated retreat of sea ice, deterioration of the Southern Ocean halocline, and poleward shift in
269 the westerlies. These changes then led to the release of CO_2 from the deep ocean (*87*) which
270 combined with obliquity (Fig. 4D) to fully deglaciate NH ice sheets and usher in the next
271 interglaciation.

Contrasting temperature and ice-sheet responses to CO_2 forcing over the past 0.8 Myr are clearly expressed in their variance spectra, with a dominant ~100-kyr cycle in GMST (*21*) that is shared by CO_2 (fig. S9A) whereas the concentration of GMSL variance is nearly equally distributed between 41 kyr and ~100 kyr (Fig. 2B, fig. S9B). Insofar as the variance characteristics of GMST are shared by GMSST, MOT, and thus $\delta^{18}O_T$ (*92*) and those of GMSL are shared by $\delta^{18}O_{sw}$, we can similarly evaluate the relative contributions of $\delta^{18}O_T$ and $\delta^{18}O_{sw}$ to the variance of the $\delta^{18}O_b$ record since the MPT. The $\delta^{18}O_b$ record has long been used to argue that the dominant post-MPT ~100-kyr signal in that record (Fig. 5A) is from ice-sheet dynamics (*8, 14, 93-95*), but our results show that its origin is largely in the $\delta^{18}O_T$ component due to changes in the carbon cycle (Fig. 5B), as first recognized by Ref. (*75*). Overall, however, terminations present in both $\delta^{18}O_T$ and $\delta^{18}O_{sw}$ were set by the threshold of when ice sheets exceeded a limiting size beyond which they responded nonlinearly to obliquity forcing and helped drive a termination. This threshold was reached for nearly every obliquity cycle of the Pleistocene prior to the MPT (Fig. 3D, 3E). Afterward, the development of the ~100-kyr cycle arising from the long-term cooling enhanced the ability of the Southern Ocean carbon cycle to sequester CO_2 and modulate the response of $\delta^{18}O_T$ and $\delta^{18}O_{sw}$ to obliquity forcing until the growth of the next large ice sheet.

Conclusions

We find that between 4.5 and 3 Ma, sea-level highstands remained ~20 m above present suggesting large decreases in AIS and GrIS volume relative to today. Beginning at 4 Ma, sea-level lowstands began to episodically extend below present by as much as -50 to -80 m suggesting the onset of Northern Hemisphere (NH) glaciation. Sustained intensification of NH glaciation occurred from 3 Ma to 2.5 Ma, with highstands decreasing to near-modern levels while lowstands

294 decreased to levels comparable to or lower than the Last Glacial Maximum (LGM) lowstand ~21
295 ka that continued throughout much of the Pleistocene.

296 Our finding that large ice sheets existed throughout the Pleistocene modifies as well as
297 adds several fundamental challenges to our understanding of ice sheet-climate interactions and
298 their joint responses to external forcing. Underlying each of these challenges is the fact that the
299 dominant orbital-scale GMSL variability and its changes over the past 3 Myr is not the one that
300 would be predicted by the associated orbital forcing, suggesting internal feedbacks of the climate
301 system that we propose are largely driven by changes in the Southern Ocean carbon cycle and their
302 effect on $[CO_2]_{atm}$ and GMST. High-resolution ice-core CO_2 records that extend beyond 0.8 Ma
303 are needed to test our hypotheses. Finally, the presence of large ice sheets throughout the MPT
304 indicates that the hypothesis of regolith removal to explain the change in ice-sheet sensitivity to
305 orbital forcing (*5, 48*) can be rejected.
306

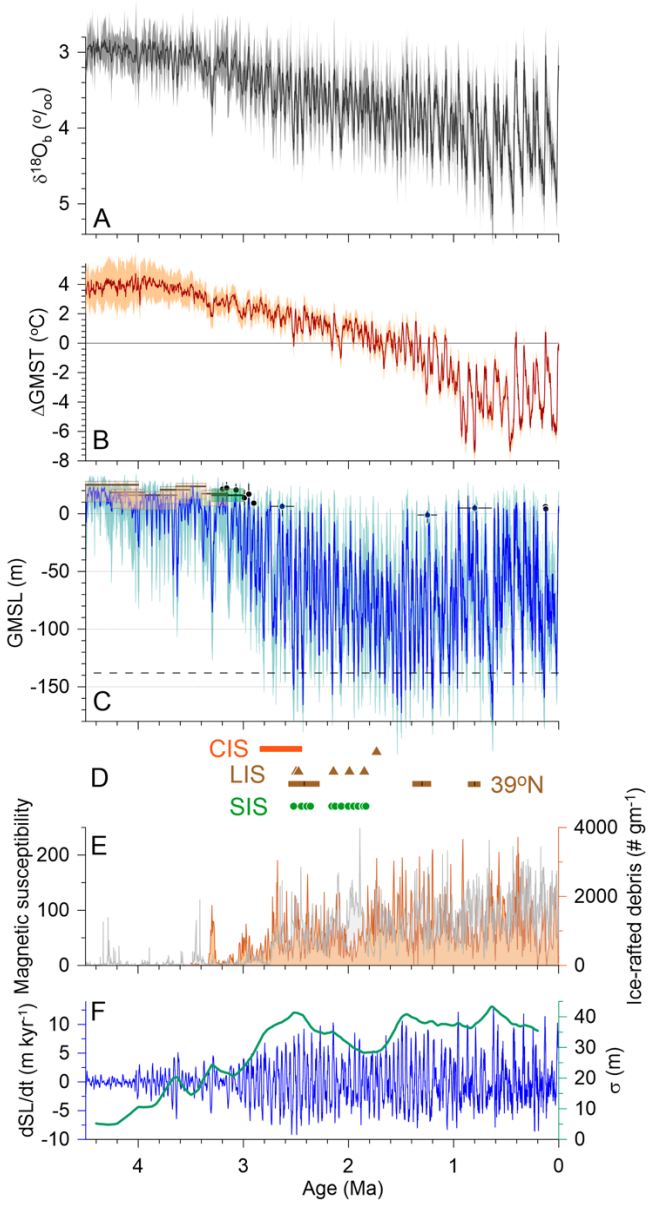

307

308 **Fig. 1**. **Global mean temperature and sea-level changes over the past 4.5 Myr.** (**A**) Prob-stack
309 $\delta^{18}O_b$ record (*12*). (**B**) Global mean surface temperature difference (ΔGMST) (brick red with 1σ
310 uncertainty) referenced to PI. (**C**) Global mean sea level (GMSL) (blue line with 1σ uncertainty).
311 Also shown are published Pliocene (*34-36*) and Pleistocene (*96, 97*) sea-level highstands. Dashed
312 horizontal line is referenced to the LGM lowstand (-130 m). (**D**) Geologic evidence of extensive
313 margins of early-to-middle Pleistocene Cordilleran Ice Sheet (CIS, orange symbols) (*40*),
314 Laurentide Ice Sheet records at 39°N (LIS, brown symbols) (*39, 41*), and Scandinavian Ice Sheet
315 (SIS, green symbols) (*43*). Newer evidence suggests a more-limited extent of the SIS in the North
316 Sea prior to 1.1 Ma (*98*) than inferred by Ref. (*43*), but the difference in extent, and its contribution
317 to GMSL, is negligible. (**E**) Records of ice-rafted debris from the North Pacific (gray) (*45*) and
318 Nordic Seas (orange) (*44*). (**F**) Rate of change (12-kyr running average) (dark blue line) and
319 standard deviation (σ, 200-kyr centered) (green line) of GMSL.

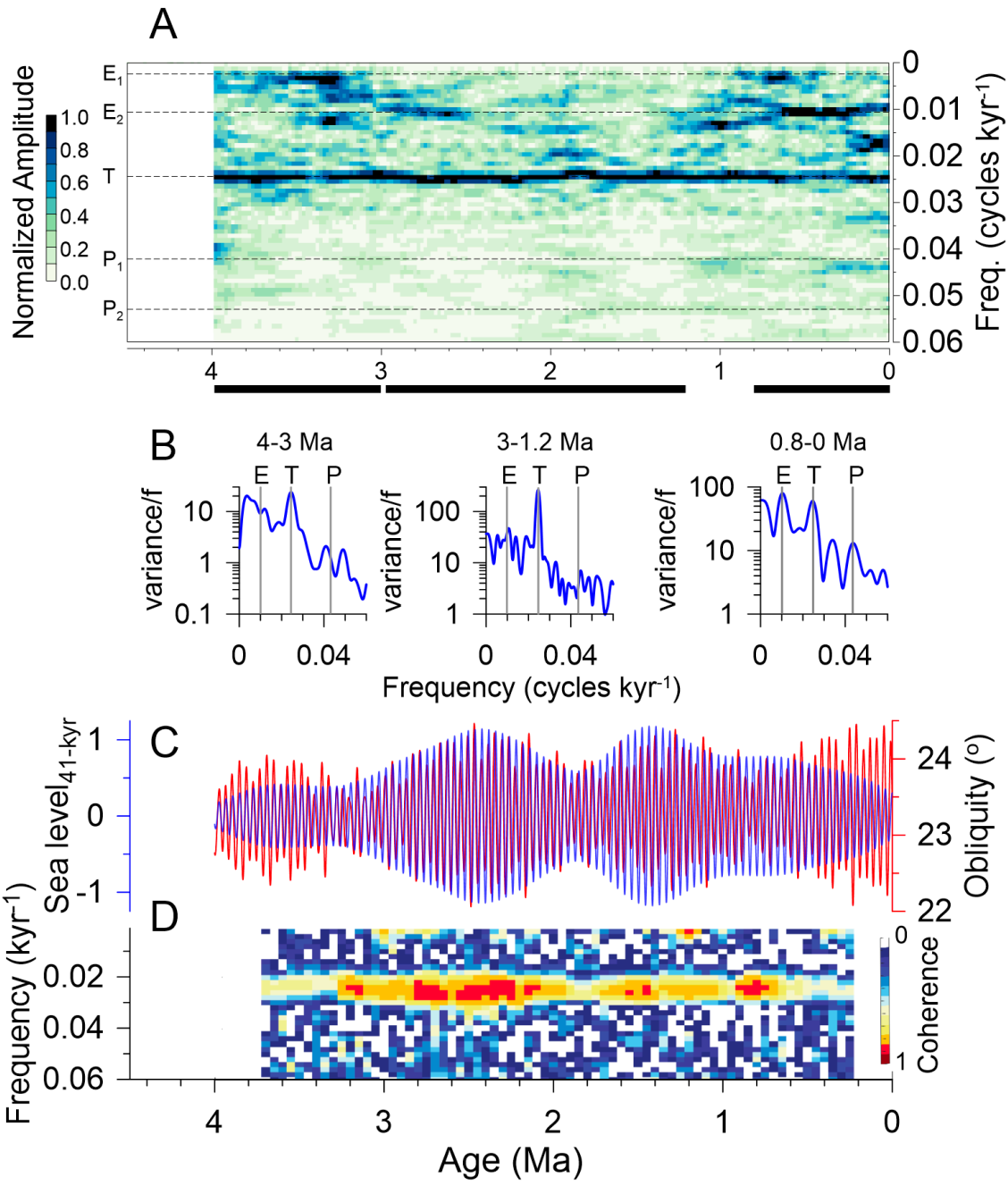

Fig. 2. Spectral characteristics of global mean sea level. (**A**) Evolutionary spectra of global mean sea level (GMSL). The dominant periods in insolation variations at orbital periods are indicated by horizontal lines (eccentricity: E_1 = 400 kyr, E_2 = 96 kyr; obliquity: T = 41 kyr and precession: P_1 = 23 kyr, P_2 = 19 kyr). (**B**) Spectral density of GMSL (variance per frequency) for three periods corresponding to horizontal black bars shown in (**A**) (3-4 Ma, 1.2-3 Ma, 0-0.8 Ma). Orbital periods are indicated by vertical lines (E = eccentricity (96 kyr), T = obliquity (41 kyr), and P = precession (23 kyr)). Note scale change for y-axes (variance/f). (**C**) Filtered GMSL using a 41-kyr filter (blue line) and obliquity (black line). (**D**) Coherence between 41-kyr filtered GMSL and obliquity.

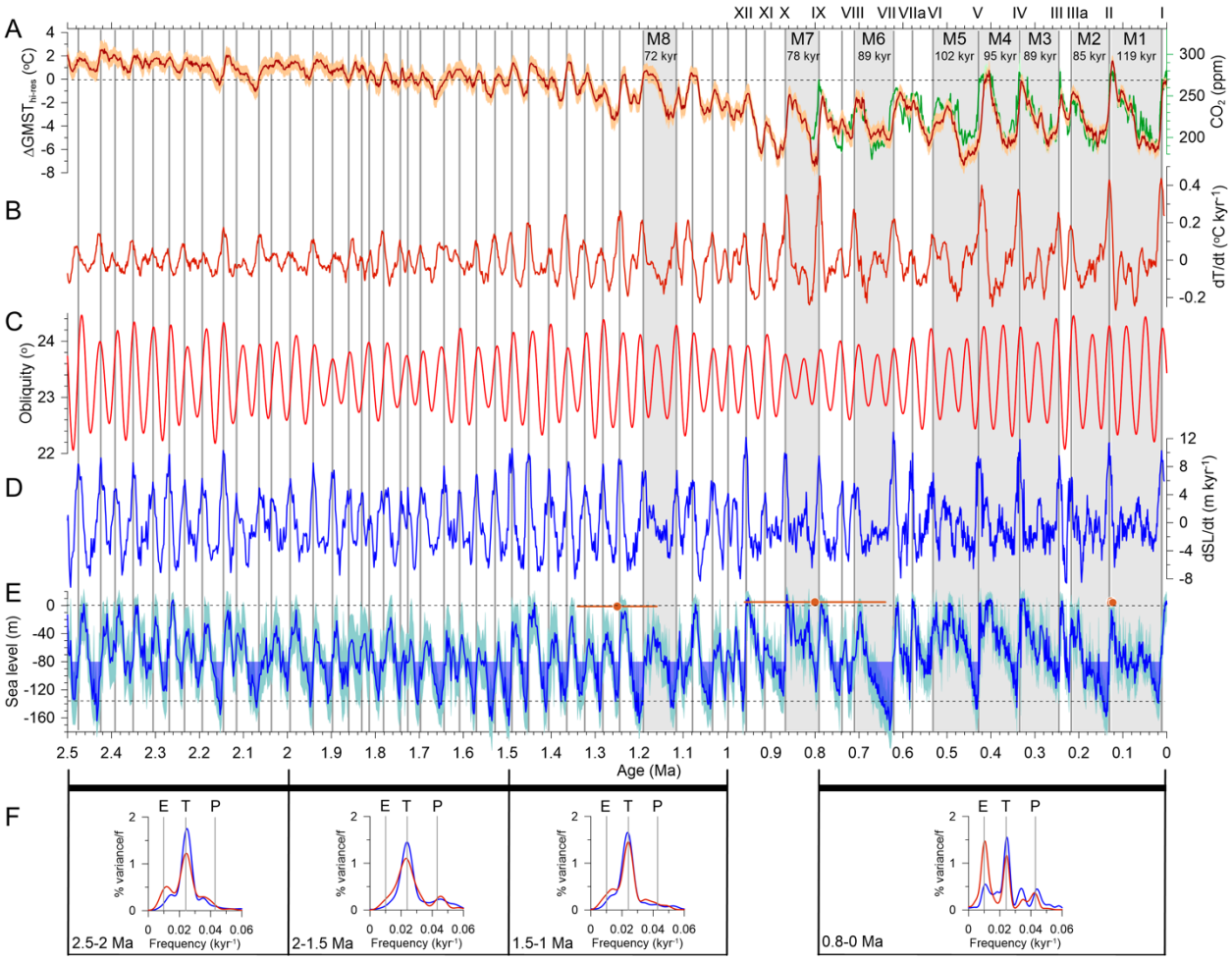

330

331

332 **Fig. 3**. **Global temperature and sea-level changes over the past 2.5 Myr.** (**A**) Global mean
333 surface temperature change (ΔGMST) (brick red with 1σ uncertainty,) referenced to PI, and
334 atmospheric CO_2 (green) (*99*) placed on the AICC2023 chronology (*100*). (**B**) Rate of change of
335 ΔGMST. (**C**) Obliquity (*68*). (**D**) Rate of change of global mean sea level (GMSL) (12-kyr running
336 average), whose maxima are highlighted by vertical lines across **(A-E)**. (**E**) Global mean sea level.
337 Sea-level threshold of -80 m that, when exceeded, is followed by a termination upon next increase
338 in obliquity (see text) is shown by filled blue sea-level intervals. Dashed horizontal lines
339 correspond to present (0 m) and LGM (-130 m) sea levels. Brick-red symbols with 1σ age
340 uncertainty are published Pleistocene sea-level highstands (*96, 97*). (**F**) Spectral density of rate of
341 change of ΔGMST (brick red) and GMSL (blue) for four periods corresponding to horizontal black
342 bars shown in (**E**). Eccentricity (E, 100-kyr), tilt (T, 41-kyr) and precession (P, 23-kyr) frequency
343 bands noted by vertical lines.

344

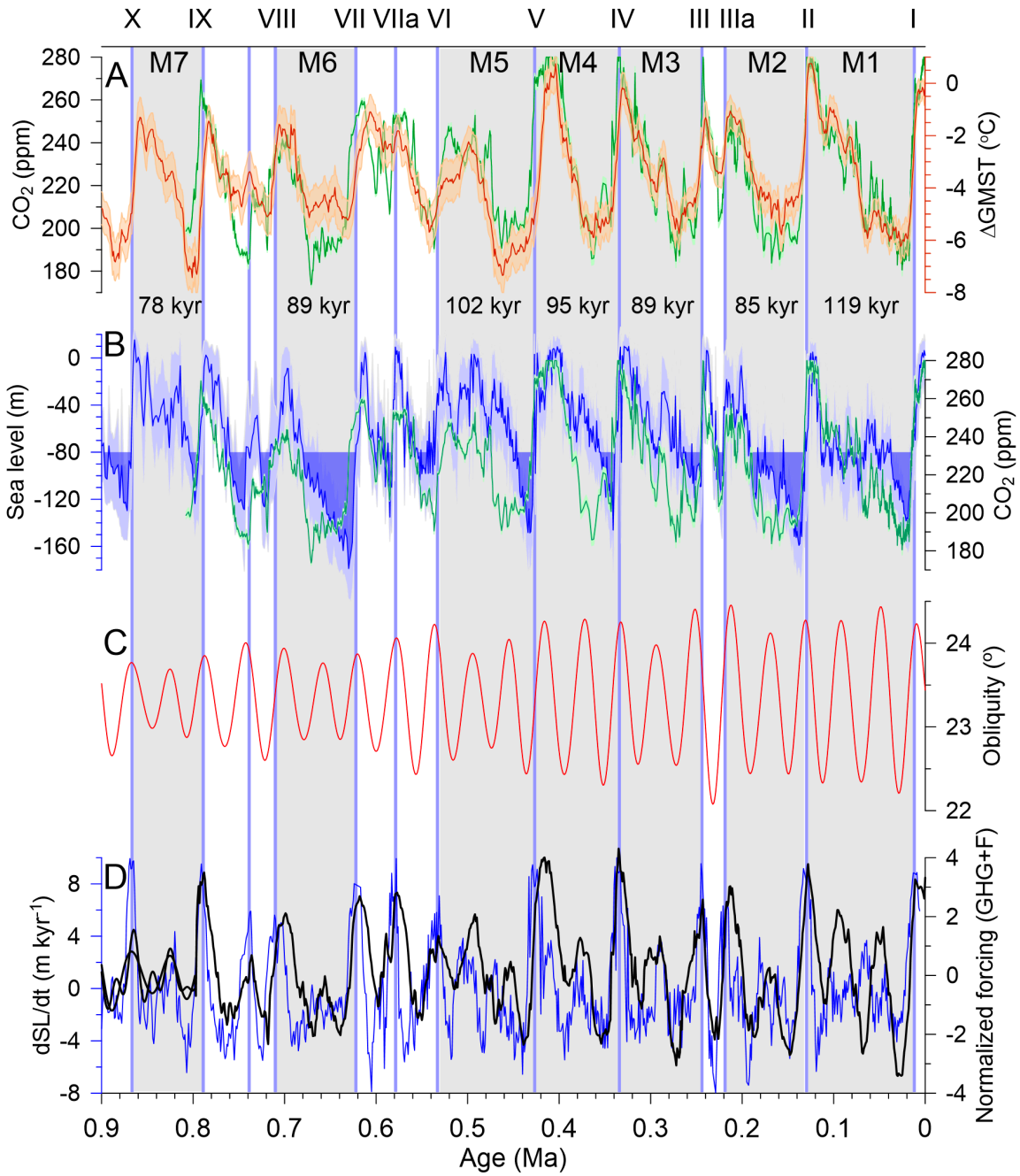

Fig. 4. **Assessing the origin of the ~100-kyr cycle.** (**A**) Global mean surface temperature change (ΔGMST) (brick red) referenced to PI, and atmospheric CO_2 (green) (*99*) both with 1σ uncertainty. (**B**) Global mean sea level (GMSL) (blue) and atmospheric CO_2 (green) (*99*), both with 1σ uncertainty. (**C**) Obliquity (*68*). (**D**) Rate of change of GMSL (blue) compared to a normalized forcing function F (GHG+*F*) (*101*) that combines normalized atmospheric CO_2 from the Antarctic ice-core record over the past 0.8 Myr (black) (*99*) placed on the AICC2023 chronology (*100*) and normalized obliquity. Note that there is no significant improvement in the correlation between rate of change of GMSL and a forcing function that combines various proportions of precession and obliquity (5:95, 25:75, 50:50).

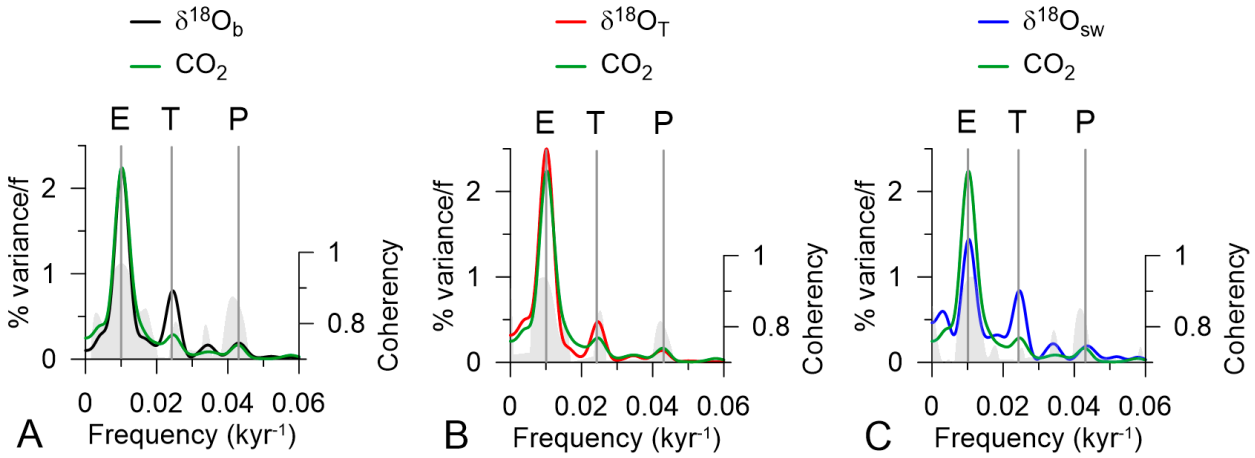

Fig. 5. Spectral density of the $\delta^{18}O_b$ record, its components, and atmospheric CO_2 for past 0.8 Myr. (**A**) Spectral density (normalized variance) of the Prob-stack $\delta^{18}O_b$ record (*12*) and atmospheric CO_2 (green) (*99*). (**B**) Spectral density (normalized variance) of the temperature component ($\delta^{18}O_T$) of the $\delta^{18}O_b$ record (*18*) and atmospheric CO_2 (green) (*99*). (**C**) Spectral density (normalized variance) of the seawater component ($\delta^{18}O_{sw}$) of the $\delta^{18}O_b$ record (*18*) and atmospheric CO_2 (green) (*99*).

REFERENCES AND NOTES

1. T. Westerhold *et al.*, An astronomically dated record of Earth's climate and its predictability over the last 66 million years. *Science* **369**, 1383-1387 (2020).
2. J. Zachos, M. Pagani, L. Sloan, E. Thomas, K. Billups, Trends, rhythms, and aberrations in global climate 65 Ma to present. *Science* **292**, 686-693 (2001).
3. N. J. Shackleton, N. D. Opdyke*,* R. M. Cline, J. D. Hays, Eds. (Geological Society of America Memoir, Boulder, CO, 1976), vol. 145, pp. 449-464.
4. N. G. Pisias, T. C. Moore, Jr., The evolution of Pleistocene climate: a time series approach. *Earth and Planetary Science Letters* **52**, 450-458 (1981).
5. P. U. Clark *et al.*, The middle Pleistocene transition: Characteristics. mechanisms, and implications for long-term changes in atmospheric PCO2. *Quaternary Science Reviews* **25**, 3150-3184 (2006).
6. J. D. Hays, J. Imbrie, N. J. Shackleton, Variations in the Earth's orbit: Pacemaker of the ice ages. *Science* **194**, 1121-1132 (1976).
7. J. Imbrie *et al.*, On the structure and origin of major glaciation cycles 1. Linear responses to Milankovitch forcing. *Paleoceanography* **7**, 701-738 (1992).
8. J. Imbrie *et al.*, On the structure and origin of major glaciation cycles. 2. The 100,000-year cycle. *Paleoceanography* **8**, 699-735 (1993).
9. J. Hansen, M. Sato, G. Russell, P. Kharecha, Climate sensitivity, sea level and atmospheric carbon dioxide. *Philosophical Transactions of the Royal Society A-Mathematical Physical and Engineering Sciences* **371**, 10.1098/rsta.2012.0294 (2013).
10. N. G. Pisias *et al.*, High resolution stratigraphic correlation of benthic oxygen isotopic records spanning the last 300,000 years. *Marine Geology,* **56**, 119-136 (1984).
11. L. E. Lisiecki, M. E. Raymo, A Pliocene-Pleistocene stack of 57 globally distributed benthic $\delta^{18}O$ records. *Paleoceanography* **20**, 2004PA001071 (2005).
12. S. Ahn, D. Khider, L. E. Lisiecki, C. E. Lawrence, A probabilistic Pliocene–Pleistocene stack of benthic $\delta^{18}O$ using a profile hidden Markov model. *Dynamics and Statistics of the Climate System* **2**, 1-16 (2017).
13. P. Huybers, Glacial variability over the last two million years: an extended depth-derived age model, continuous obliquity pacing, and the Pleistocene progression. *Quaternary Science Reviews* **26**, 37-55 (2007).
14. P. Bajo *et al.*, Persistent influence of obliquity on ice age terminations since the Middle Pleistocene transition. *Science* **367**, 1235-1239 (2020).
15. M. E. Raymo, R. Kozdon, D. Evans, L. Lisiecki, H. L. Ford, The accuracy of mid-Pliocene $\delta^{18}O$-based ice volume and sea level reconstructions. *Earth-Science Reviews* **177**, 291-302 (2018).
16. D. P. Schrag, Effects of diagenesis on the isotopic record of late Paleogene tropical sea surface temperatures. *Chemical Geology* **161**, 215-224 (1999).
17. H. J. Spero, J. Bijma, D. W. Lea, B. E. Bemis, Effect of seawater carbonate concentration on foraminiferal carbon and oxygen isotopes. *Nature* **390**, 497-500 (1997).
18. P. U. Clark *et al.*, Mean ocean temperature change and decomposition of the benthic d18O record over the last 4.5 Myr. *EGUsphere* **2024**, 1-41 (2024).
19. M. J. Winnick, J. K. Caves, Oxygen isotope mass-balance constraints on Pliocene sea level and East Antarctic Ice Sheet stability. *Geology* **43**, 879-882 (2015).

20. E. Gasson, R. M. DeConto, D. Pollard, Modeling the oxygen isotope composition of the Antarctic ice sheet and its significance to Pliocene sea level. *Geology* **44**, 827-830 (2016).
21. P. U. Clark, J. D. Shakun, Y. Rosenthal, P. Köhler, P. J. Bartlein, Global and regional temperature change over the last 4.5 million years. *Science* **383**, 884-890 (2024).
22. K. G. Miller *et al.*, Cenozoic sea-level and cryospheric evolution from deep-sea geochemical and continental margin records. *Science Advances* **6**, (2020).
23. J. D. Shakun, D. W. Lea, L. E. Lisiecki, M. E. Raymo, An 800-kyr record of global surface ocean delta O-18 and implications for ice volume-temperature coupling. *Earth and Planetary Science Letters* **426**, 58-68 (2015).
24. C. Waelbroeck *et al.*, Sea-level and deep water temperature changes derived from benthic foraminifera isotopic records. *Quaternary Science Reviews* **21**, 295-305 (2002).
25. S. L. Bates, M. Siddall, C. Waelbroeck, Hydrographic variations in deep ocean temperature over the mid-Pleistocene transition. *Quaternary Science Reviews* **88**, 147-158 (2014).
26. K. A. Jakob *et al.*, A new sea-level record for the Neogene/Quaternary boundary reveals transition to a more stable East Antarctic Ice Sheet. *Proceedings of the National Academy of Sciences of the United States of America* **117**, 30980-30987 (2020).
27. E. J. Rohling *et al.*, Comparison and synthesis of sea-level and deep-sea temperature variations over the past 40 million years. *Reviews of Geophysics* **60**, e2022RG000775 (2022).
28. E. J. Rohling *et al.*, Sea level and deep-sea temperature reconstructions suggest quasi-stable states and critical transitions over the past 40 million years. *Science Advances* **7**, eabf5326 (2021).
29. M. A. Maslin, X. S. Li, M. F. Loutre, A. Berger, The contribution of orbital forcing to the progressive intensification of Northern Hemisphere glaciation. *Quaternary Science Reviews* **17**, 411-426 (1998).
30. H. Cheng *et al.*, Ice Age Terminations. *Science* **326**, 248-252 (2009).
31. H. Cheng *et al.*, The Asian monsoon over the past 640,000 years and ice age terminations. *Nature* **534**, 640-646 (2016).
32. P. C. Tzedakis, M. Crucifix, T. Mitsui, E. W. Wolff, A simple rule to determine which insolation cycles lead to interglacials. *Nature* **542**, 427-432 (2017).
33. P. Köhler, R. S. W. van de Wal, Interglacials of the Quaternary defined by northern hemispheric land ice distribution outside of Greenland. *Nature Communications* **11**, 11:5124 (2020).
34. O. A. Dumitru *et al.*, Constraints on global mean sea level during Pliocene warmth. *Nature* **574**, 233-236 (2019).
35. K. G. Miller *et al.*, High tide of the warm Pliocene: Implications of global sea level for Antarctic deglaciation. *Geology* **40**, 407-410 (2012).
36. F. D. Richards *et al.*, Geodynamically corrected Pliocene shoreline elevations in Australia consistent with midrange projections of Antarctic ice loss. *Science Advances* **9**, (2023).
37. G. S. Dwyer, M. A. Chandler, Mid-Pliocene sea level and continental ice volume based on coupled benthic Mg/Ca palaeotemperatures and oxygen isotopes. *Philosophical Transactions of the Royal Society A-Mathematical Physical and Engineering Sciences* **367**, 157-168 (2009).
38. S. Sosdian, Y. Rosenthal, Deep-sea temperature and ice volume changes across the Pliocene-Pleistocene climate transitions. *Science* **325**, 306-310 (2009).

39. G. Balco, C. W. Rovey, Absolute chronology for major Pleistocene advances of the Laurentide Ice Sheet. *Geology* **38**, 795-798 (2010).
40. A. J. Hidy, J. C. Gosse, D. G. Froese, J. D. Bond, D. H. Rood, A latest Pliocene age for the earliest and most extensive Cordilleran Ice Sheet in northwestern Canada. *Quaternary Science Reviews* **61**, 77-84 (2013).
41. J. D. Shakun, M. E. Raymo, D. W. Lea, An early Pleistocene Mg/Ca-δ^{18}O record from the Gulf of Mexico: Evaluating ice sheet size and pacing in the 41-kyr world. *Paleoceanography* **31**, 1011-1027 (2016).
42. K. Blake-Mizen *et al.*, Southern Greenland glaciation and Western Boundary Undercurrent evolution recorded on Eirik Drift during the late Pliocene intensification of Northern Hemisphere glaciation. *Quaternary Science Reviews* **209**, 40-51 (2019).
43. B. R. Rea *et al.*, Extensive marine-terminating ice sheets in Europe from 2.5 million years ago. *Science Advances* **4**, eaar8327 (2018).
44. E. Jansen, T. Fronval, F. Rack, J. E. T. Channell, Pliocene-Pleistocene ice rafting history and cyclicity in the Nordic Seas during the last 3.5 Myr. *Paleoceanography* **15**, 709-721 (2000).
45. G. H. Haug, D. M. Sigman, R. Tiedemann, T. F. Pedersen, M. Sarnthein, Onset of permanent stratification in the subarctic Pacific Ocean. *Nature* **401**, 779-782 (1999).
46. N. J. Shackleton, N. D. Opdyke, Oxygen isotope and paleomagnetic evidence for early Northern Hemisphere glaciation. *Nature* **270**, 216-219 (1977).
47. M. E. Raymo, The initiation of Northern Hemisphere glaciation. *Annual Review of Earth Planetary Sciences,* **22**, 353-383 (1994).
48. P. U. Clark, D. Pollard, Origin of the middle Pleistocene transition by ice sheet erosion of regolith. *Paleoceanography* **13**, 1-9 (1998).
49. M. E. Raymo, K. Nisancioglu, The 41 kyr world: Milankovitch's other unsolved mystery. *Paleoceanography* **18**, 2002PA000791 (2003).
50. P. Huybers, E. Tziperman, Integrated summer insolation forcing and 40,000-year glacial cycles: The perspective from an ice-sheet/energy-balance model. *Paleoceanography* **23**, PA1208 (2008).
51. C. R. Tabor, C. J. Poulsen, D. Pollard, How obliquity cycles powered early Pleistocene global ice-volume variability. *Geophysical Research Letters* **42**, 1871-1879 (2015).
52. J. Boellstorff, North American Pleistocene stages reconsidered in light of probably Pliocene-Pleistocene continental glaciation. *s* **202**, 305-307 (1978).
53. M. E. Raymo, L. E. Lisiecki, K. H. Nisancioglu, Plio-Pleistocene ice volume, Antarctic climate, and the global delta O-18 record. *Science* **313**, 492-495 (2006).
54. K. A. Dyez, B. Honisch, G. A. Schmidt, Early Pleistocene Obliquity-Scale pCO(2) Variability at similar to 1.5 Million Years Ago. *Paleoceanography and Paleoclimatology* **33**, 1270-1291 (2018).
55. Z. Liu, H. Yang, Extratropical control of tropical climate, the atmospheric bridge and oceanic tunnel. *Geophysical Research Letters* **30**, 1-4 (2003).
56. S. Y. Lee, C. J. Poulsen, Sea ice control of Plio-Pleistocene tropical Pacific climate evolution. *Earth and Planetary Science Letters* **248**, 253-262 (2006).
57. T. D. Herbert, L. C. Peterson, K. T. Lawrence, Z. Liu, Tropical ocean temperatures over the past 3.5 million years. *Science* **328**, 1530-1534 (2010).
58. P. Huybers, P. Molnar, Tropical cooling and the onset of North American glaciation. *Climate of the Past* **3**, 549-557 (2007).

59. P. U. Clark, S. W. Hostetler, N. G. Pisias, A. Schmittner, K. J. Meissner, in *Ocean Circulation: Mechanisms and Impacts,* A. Schmittner, J. Chiang, S. Hemming, Eds. (American Geophysical Union, Geophysical Monograph, 2007), vol. 173, pp. 209-246.
60. M. P. Erb, C. S. Jackson, A. J. Broccoli, Using Single-Forcing GCM Simulations to Reconstruct and Interpret Quaternary Climate Change. *Journal of Climate* **28**, 9746-9767 (2015).
61. J. Fyke, O. Sergienko, M. Lofverstrom, S. Price, J. T. M. Lenaerts, An overview of interactions and feedbacks between ice sheets and the Earth system. *Reviews of Geophysics* **56**, 361-408 (2018).
62. X. Li *et al.*, Mid-Pliocene westerlies from PlioMIP simulations. *Advances in Atmospheric Sciences* **32**, 909-923 (2015).
63. S. Hofer, A. J. Tedstone, X. Fettweis, J. L. Bamber, Decreasing cloud cover drives the recent mass loss on the Greenland Ice Sheet. *Science Advances* **3**, (2017).
64. N. Sagoo *et al.*, Observationally Constrained Cloud Phase Unmasks Orbitally Driven Climate Feedbacks. *Geophysical Research Letters* **48**, (2021).
65. N. Unger, X. Yue, Strong chemistry- climate feedbacks in the Pliocene. *Geophysical Research Letters* **41**, 527-533 (2014).
66. D. Pollard, S. L. Thompson, Climate and ice-sheet mass balance at the Last Glacial Maximum from GENESIS version 2 global climate model. *Quaternary Science Reviews* **16**, 841-863 (1997).
67. S. L. Thompson, D. Pollard, Greenland and Antarctic mass balances for present and doubled atmospheric CO2 from the GENESIS version-2 global climate model. *Journal of Climate* **10**, 871-900 (1997).
68. J. Laskar *et al.*, A long term numerical solution for the insolation quantities of the Earth. *Astronomy and Astrophysics* **428**, 261-285 (2004).
69. P. Köhler, Atmospheric CO_2 concentration based on boron isotopes versus simulations of the global carbon cycle during the Plio-Pleistocene. *Paleoceanography and Paleoclimatology* **38**, e2022PA004439 (2023).
70. A. Berger, X. S. Li, M. F. Loutre, Modelling northern hemisphere ice volume over the last 3 Ma. *Quaternary Science Reviews* **18**, 1-11 (1999).
71. M. Willeit, A. Ganopolski, R. Calov, V. Brovkin, Mid-Pleistocene transition in glacial cycles explained by declining CO_2 and regolith removal. *Science Advances* **5**, eaav7337 (2019).
72. E. Tziperman, H. Gildor, On the mid-Pleistocene transition to 100-kyr glacial cycles and the asymmetry between glaciation and deglaciation times. *Paleoceanography* **18**, PA000627 (2003).
73. P. Huybers, C. Wunsch, Obliquity pacing of the late Pleistocene glacial terminations. *Nature* **434**, 491-494 (2005).
74. T. B. Chalk *et al.*, Causes of ice age intensification across the Mid-Pleistocene Transition. *Proceedings of the National Academy of Sciences* **114**, 13114-13119 (2017).
75. N. J. Shackleton, The 100,000 year Ice-Age cycle identified and found to lag temperature, carbon dioxides and orbital eccentricity. *Science* **289**, 1897-1902 (2000).
76. J. Imbrie, J. Z. Imbrie, Modeling the climatic response to orbital variations. *Science* **207**, 943-953 (1980).
77. A. Abe-Ouchi *et al.*, Insolation-driven 100,000-year glacial cycles and hysteresis of ice-sheet volume. *Nature* **500**, 190-193 (2013).

78. D. Pollard, A simple ice sheet model yields realistic 100 kyr glacial cycles. *n* **296**, 334-338 (1982).
79. P. U. Clark, R. B. Alley, D. Pollard, Northern Hemisphere ice-sheet influences on global climate change. *Science* **286**, 1104-1111 (1999).
80. W. F. Ruddiman, M. E. Raymo, D. G. Martinson, B. M. Clement, J. Backman, Pleistocene evolution: northern hemisphere ice sheets and North Atlantic ocean. *Paleoceanography* **4**, 353-412 (1989).
81. D. M. Sigman *et al.*, The Southern Ocean during the ice ages: A review of the Antarctic surface isolation hypothesis, with comparison to the North Pacific. *Quaternary Science Reviews* **254**, (2021).
82. A. Martinez-Garcia *et al.*, Southern Ocean dust-climate coupling over the past four million years. *Nature* **476**, 312-315 (2011).
83. A. P. Hasenfratz *et al.*, The residence time of Southern Ocean surface waters and the 100,000-year ice age cycle. *Science* **363**, 1080-1084 (2019).
84. R. Ferrari *et al.*, Antarctic sea ice control on ocean circulation in present and glacial climates. *Proceedings of the National Academy of Sciences* **111**, 8753-8758 (2014).
85. M. F. Jansen, Glacial ocean circulation and stratification explained by reduced atmospheric temperature. *Proceedings of the National Academy of Sciences* **114**, 45-50 (2017).
86. A. Marzocchi, M. F. Jansen, Global cooling linked to increased glacial carbon storage via changes in Antarctic sea ice. *Nature Geoscience* **12**, 1001-1005 (2019).
87. P. Köhler, R. Bintanja, The carbon cycle during the Mid Pleistocene Transition: the Southern Ocean decoupling hypothesis. *Climate of the Past* **4**, 311-332 (2008).
88. D. Pollard, A coupled climate-ice sheet model applied to the Quaternary ice ages. *Journal of Geophysical Research* **88**, 7705-7718 (1983).
89. S. J. Marshall, P. U. Clark, Basal temperature evolution of North American ice sheets and implications for the 100-kyr cycle. *Geophysical Research Letters* **29**, GL015192 (2002).
90. P. U. Clark *et al.*, Oceanic forcing of penultimate deglacial and last interglacial sea-level rise. *Nature* **577**, 660-664 (2020).
91. M. E. Raymo, The timing of major climate terminations. *Paleoceanography* **12**, 577-585 (1997).
92. P. U. Clark *et al.*, Mean ocean temperature change and decomposition of the benthic $d^{18}O$ record over the last 4.5 Myr. *Climate of the Past*, (in review).
93. W. S. Broecker, J. van Donk, Insolation changes, ice volumes, and the O-18 record in deep-sea cores. *Reviews of Geophysics and Space Physics* **8**, 169-198 (1970).
94. N. J. Shackleton, The oxygen isotope stratigraphic record of the Late Pleistocene. *Philosophical Transactions Royal Society of London* **280B**, 169-182 (1977).
95. S. Barker *et al.*, Persistent influence of precession on northern ice sheet variability since the early Pleistocene. *Science* **376**, 961-+ (2022).
96. O. A. Dumitru *et al.*, Sea-level stands from the Western Mediterranean over the past 6.5 million years. *Sci Rep-Uk* **11**, 6681 (2021).
97. A. Dutton, J. M. Webster, D. Zwartz, K. Lambeck, B. Wohlfarth, Tropical tales of polar ice: evidence of Last Interglacial polar ice sheet retreat recorded by fossil reefs of the granitic Seychelles islands. *Quaternary Science Reviews* **107**, 182-196 (2015).
98. D. Ottesen, C. L. Batchelor, H. Loseth, H. Brunstad, 3D seismic evidence for a single Early Pleistocene glaciation of the central North Sea. *Science Advances* **10**, eadq6089 (2024).

592 99. B. Bereiter *et al.*, Revision of the EPICA Dome C CO_2 record from 800 to 600kyr before
593 present. *Geophysical Research Letters* **42**, 542-549 (2015).
594 100. M. Bouchet *et al.*, The Antarctic Ice Core Chronology 2023 (AICC2023) chronological
595 framework and associated timescale for the European Project for Ice Coring in Antarctica
596 (EPICA) Dome C ice core. *Clim. Past* **19**, 2257-2286 (2023).
597 101. P. Huybers, Combined obliquity and precession pacing of late Pleistocene deglaciations.
598 *Nature* **480**, 229-232 (2011).
599

600

Acknowledgments: This publication contributed to Beyond EPICA, a project of the European Union's Horizon 2020 research and innovation program (Oldest Ice Core).

Funding:

National Science Foundation OPP-2103032 (PUC)

University of Oregon Fund for Faculty Excellence (PB)

National Science Foundation OCE-1810681 (ZL)

National Science Foundation OCE-1834208 (YR)

Author contributions:

Conceptualization: PUC, JDS

Methodology: JDS, YR, DP, SWH, PUC, PJB, NGP

Investigation: PUC, JDS, YR, DP, SWH, PK, PJB

Writing – original draft: PUC

Writing – review & editing: PUC, JDS, YR, DP, SWH, PK, PJB, JMG, DPS, CZ, ZL, NGP

Competing interests: Authors declare that they have no competing interests.

Data Availability Statement: All data are available in the supplementary materials.

Supplementary Materials

Materials and Methods

Figs. S1 to S10

Table S1

References (XX-XX)

Supplementary Materials for

Global sea level over the past 4.5 million years

Peter U. Clark *et al.*

Corresponding author: Peter U. Clark, clarkp@onid.orst.edu

This PDF file includes:

- Materials and Methods
- Figs. S1 to S10
- Table S1
- References (XX-XX)

Other Supplementary Material for this manuscript includes the following:

- Data S1

1. Assessment of GMSL reconstructions

Two different approaches have been used to decompose the $\delta^{18}O$ record measured in benthic foraminifera ($\delta^{18}O_b$) into its two primary components: the temperature ($\delta^{18}O_T$) and the $\delta^{18}O$ of seawater ($\delta^{18}O_{sw}$) that the benthic foraminifera shells formed in, with the latter largely reflecting sea level. Ref. (*1*) developed an approach that regresses independently known sea-level data (e.g., from corals) on $\delta^{18}O_b$ for the last glacial cycle and then uses this regression to reconstruct sea level from $\delta^{18}O_b$ records for the last four glacial cycles. Sea level is then converted to $\delta^{18}O_{sw}$ using a constant relation of $\Delta\delta^{18}O_{sw}$:ΔGMSL. Refs. *(2)* and *(3)* extended the regression over the last two glacial cycles to reconstruct sea level from $\delta^{18}O_b$ records over the last 5 Myr (figs. S1B, S6C). Refs. (*4, 5*) further extended the regression over the last 800 kyr using the LR04 $\delta^{18}O_b$ stack and a stack of sea-level records from Ref. (*6*) (fig. S7C) to reconstruct sea level over the last 40 Myr (figs. S1B and S6A show last 4.5 Myr). Refs. (*4, 5*) also accounted for $\delta^{18}O$ variations in land ice ($\delta^{18}O_i$) over the last glacial cycle which they then applied to their sea-level record to derive $\delta^{18}O_{sw}$ from $\delta^{18}O_b$, but this did not include the effect of increasing temperatures on $\delta^{18}O_i$ prior to 0.8 Ma. In any event, applying this regression approach to a $\delta^{18}O_b$ record will, by default, reproduce the variability of the $\delta^{18}O_b$ record, including the increase in the size of glaciations during the mid-Pleistocene transition (MPT), with the early Pleistocene low-amplitude variability further reinforced by not accounting for higher temperatures on $\delta^{18}O_i$.

Refs. (*7*) and (*8*) reconstructed sea level using a simple scaling relationship that determines the fraction of the LGM sea-level lowstand (-120 m in their case) from the fraction of the $\delta^{18}O_b$ value at any given time relative to the LGM $\delta^{18}O_b$ value. As with the regression method, this relationship reproduces the $\delta^{18}O_b$ variability throughout the Pleistocene as well as does not account for the effect of increasing temperatures on $\delta^{18}O_i$ prior to 0.8 Ma, resulting in smaller early

672 Pleistocene ice sheets than in our reconstruction (figs. S1B, S6D). Finally, these approaches imply
673 a stationary partitioning of $\delta^{18}O_b$ between temperature and ice volume, and thus do not capture the
674 larger ice volume component relative to temperature that we identify before the MPT (*9*).
675 Another approach that is similar to ours subtracts independently reconstructed seawater
676 temperature as $\delta^{18}O_T$ from $\delta^{18}O_b$ to derive $\delta^{18}O_{sw}$ (*10-15*) which can then be converted to GMSL
677 using a relation of $\Delta\delta^{18}O_{sw}$:ΔGMSL (*10, 15*). Ref. (*15*) used a reconstruction of bottom water
678 temperature (BWT) that is similar to ours in showing lower ΔBWT than ΔSST during the early
679 Pleistocene (*9*). However, this is a 2-Myr smoothed record and thus does not capture the increase
680 in orbital variability across the MPT (*9*) (figs. S1B, S6B) which contributes to larger early
681 Pleistocene ice sheets in our reconstruction. Ref. (*15*) also applied a constant 0.013‰ m^{-1}
682 relationship to derive sea level from their $\delta^{18}O_{sw}$ which does not account for the effect of warmer
683 early Pleistocene temperatures on $\delta^{18}O_i$, and thus $\delta^{18}O_{sw}$. Moreover, this relationship is more
684 appropriate for warmer climates with just the Greenland and Antarctic ice sheets (*16*) as opposed
685 to the 0.008‰ m^{-1} relationship that is more suitable for deriving sea level after 0.8 Ma.
686 Accordingly, their sea-level lowstands are generally higher than in our reconstruction throughout
687 the Pleistocene (figs. S6B, S7B).
688 Other studies that used independent orbital-scale temperature records to derive $\delta^{18}O_{sw}$ from
689 $\delta^{18}O_b$ suggest small GMSL variability in the late Pliocene that increases into the early Pleistocene
690 and continues across the MPT (*11, 17, 18*). We used our method to convert $\delta^{18}O_{sw}$ data from Refs.
691 (*11*) and (*18*) to sea level (see section 2 of this Supplementary Materials) and find generally good
692 agreement with our GMSL reconstruction (figs. S5, S6E). However, the temperature records in
693 Refs. (*11*) and (*18*) are local and so may not be representative of mean ocean temperature (MOT).

Finally, other than Refs. (*5*) and (*4*), none of the reconstructions using either approach account for changing $\delta^{18}O_i$ on $\delta^{18}O_{sw}$ (*4, 19*).

Finally, Refs. (*20, 21*) reconstructed changes in water depth using grain size variations in uplifted marine sedimentary sequences preserved in New Zealand (fig. S1, S8), with inferred water depths being supplemented by estimates from benthic foraminifera. Unconformities in the sedimentary sequence are assigned a maximum water depth of -32.5 m, and the authors assume the missing part of the sea-level record to be <5 m. Water depth is converted to relative sea level using back stripping methods that account for sediment compaction and tectonic subsidence. Their reconstruction cannot be referenced to Holocene sea level, but it does identify long-term trends as well as the frequency and amplitude of sea-level change on orbital timescales. Comparison of their reconstruction to other sea-level reconstructions (fig. S1) and to our reconstruction (fig. S8) shows a similar concentration of 41-kyr variance but disagrees with these other reconstructions in showing no trend of increasing lowstands (i.e., greater amplitude) during the intensification of Northern Hemisphere glaciation.

2. Conversion of $\delta^{18}O_{sw}$ to sea level

We develop a simple model to translate $\delta^{18}O_{sw}$ to sea level that conserves global water and ^{18}O mass as they are redistributed between the ocean and the North American (NAIS) (Laurentide and Cordilleran ice sheets), Eurasian (EUR), Greenland (GRN), and Antarctic (ANT) ice sheets. The model also accounts for the changing isotopic composition of each ice sheet through time as a function of changes in its volume and global temperature, which allows us to separate their isotopic effects. This is important because our reconstructions suggest that there is not a constant scaling between global temperature and ice volume over the past 4.5 Myr.

716 The method is based on conservation of global water and isotopic ^{18}O mass, extending
717 similar treatments in Ref. (*16*) and Ref. (*22*). A simple expression is used for the mean $\delta^{18}O$ of
718 each ice sheet as a linearized function of its size and global mean surface temperature (GMST),
719 and a parameterization is assumed for the relative size of each ice sheet to the others at all times.
720 After some tedious but straightforward algebra, this yields a quadratic equation yielding total ice
721 volume over flotation (and hence global sea-level rise) as a function of $\delta^{18}O_{sw}$ and GMST.
722 While $\delta^{18}O_{sw}$ is often converted to sea level using a constant scaling of ~-0.008 ‰/m based
723 on Last Glacial Maximum values (i.e., a ~1 ‰ $\delta^{18}O_{sw}$ enrichment (*23*) and ~130 m sea level
724 lowering (*24*)), our model accounts for time-varying temperature and ice-volume effects on ice-
725 sheet $\delta^{18}O_i$ (fig. S3D), yielding a variable relationship between $\delta^{18}O_{sw}$ and sea level (fig. S3A,
726 S3B). As a result, relative to linear scaling, applying our model to our $\delta^{18}O_{sw}$ reconstruction
727 produces lower sea levels during early Pleistocene glaciations because less-negative $\delta^{18}O_{ice}$ then
728 (due to higher temperatures) requires greater ice growth to explain $\delta^{18}O_{sw}$ enrichments, and thus
729 lower sea levels during Pliocene interglaciations because more-negative $\delta^{18}O_{ice}$ then (due to NAIS
730 and EIS absence) requires less ice loss to explain $\delta^{18}O_{sw}$ depletions (fig. S3A).
731 In the remainder of this section, we explain the details of our model. Section 2.1 derives
732 separate equations for differing climates relative to today. Section 2.2 outlines how we estimate
733 the coefficients in the expression for mean ice-sheet $\delta^{18}O$ based on observed quantities and
734 published general circulation model (GCM) experiments. Section 2.3 explains the scheme we use
735 to account for the residence time of ice in each ice sheet, and a list of prescribed quantities is given
736 in section 2.4. Finally, section 2.5 assesses the sensitivity of our sea-level reconstruction to the
737 various parameters in our model.
738 ***2.1. Equations for differing climates***

739 Separate derivations are needed for (a) generally colder time intervals when all four ice
740 sheets exist and sea level is below present (section 2.1.1), (b) generally warmer intervals when
741 ANT and GRN exist with sea level 0 to 14 m above present (section 2.1.2), and (c) much warmer
742 intervals when GRN is completely melted and only ANT exists with sea level > 14 m above present
743 (section 2.1.3). For a given pair of $\delta^{18}O_{sw}$ and GMST values, we cannot tell *a priori* which of the
744 three derivations (sections 2.1.1 to 2.1.3) is appropriate. For every pair of these values in our data
745 (with time stepping from 4.5 to 0 Ma), the quadratic solutions to the unknown K (equation 10) of
746 all three derivations were tested, always finding at most one valid real solution with computed sea
747 level within the required range for that derivation.
748 The subscript i is used below for each ice sheet (i = 1 to 4), and summation over them is
749 indicated by $\Sigma[...]$.
750 *2.1.1. Equations for generally colder climates (NAIS, EUR, GRN, ANT all larger than present; sea*
751 *level < 0 m)*
752 Starting with the conservation equations for global water and ^{18}O mass
753 $$V_{om} + \Sigma[V_{im}] = V_o + \Sigma[V_i] \quad (1)$$
754 $$V_{om}\,\delta_{om} + \Sigma[V_{im}\,\delta_{im}] = V_o\,\delta_o + \Sigma[V_i\,\delta_i] \quad (2)$$
755 where
756 V_o = ocean volume,
757 δ_o = ocean water $\delta^{18}O$, or $\delta^{18}O_{sw}$
758 V_i = volume of each ice sheet (liquid equivalent),
759 δ_i = mean $\delta^{18}O$ of each ice sheet, or $\delta^{18}O_i$
760 V_{om}, δ_{om}, V_{im}, δ_{im} are the modern values of these quantities (V_{im} = 0 for NAIS and EUR).
761 Eliminating V_o and rearranging,

$$V_{om} (\delta_{om} - \delta_o) = - \Sigma[V_{im} (\delta_{im} - \delta_o)] + \Sigma[V_i (\delta_i - \delta_o)] \quad (3)$$

We use a simple expression for the mean $\delta^{18}O$ of each ice sheet i, linearized about the modern state for ANT and GRN, or about the nascent (first-formed) ice caps for NAIS and EUR:

$$\delta_i = \alpha_i + \beta_i \Delta T - \gamma_i (V_i - V_{im}) \quad (4)$$

where α_i is the modern or nascent ice sheet $\delta^{18}O$, ΔT is the change in GMST from modern, β_i is the sensitivity to GMST with no change in volume, and γ_i is the sensitivity to ice-sheet volume with no change in GMST. Our estimates for the coefficients α_i, β_i and γ_i are given below in section 2.2.

Using (4) to eliminate δ_i in (3),

$$V_{om} (\delta_{om} - \delta_o) = - \Sigma[V_{im} (\delta_{im} - \delta_o)] + \Sigma[V_i (\alpha_i + \beta_i \Delta T - \gamma_i (V_i - V_{im}) - \delta_o)] \quad (5)$$

We need to solve (5) for V_i (all other terms are known). However, there are four unknowns (V_1, V_2, V_3, V_4) and only one equation, so three more equations are needed. For that, we assume that the proportional increase from modern towards LGM size is always the same for each ice sheet i, i.e.,

$$(V_i - V_{im}) / (V_{il} - V_{im}) = K \quad (6)$$

where V_{il} is the volume (liquid equivalent) of ice sheet i at the LGM, and K is a single number independent of ice sheet. (This only works for $K \geq 0$, i.e., for colder climates in which each ice sheet is bigger than modern). Observed or reasonably well agreed upon values of V_{il} and V_{im} are available for each ice sheet (section 2.4). Eq. (6) provides three additional independent equations, which are used with (5) to solve for K. To do that, it is useful to re-arrange (6):

$$V_i = K V_{il} + (1 - K) V_{im} \quad (7)$$

After solving for K (see below), we can recover the total ice volume:

$$\Sigma[V_i] = K \Sigma[V_{il}] + (1 - K) \Sigma[V_{im}] \quad (8a)$$

and total sea-level rise (SLR):

$$SLR \times A_o = -\Sigma[f_i (V_i - V_{im})] = -K \Sigma[f_i (V_{il} - V_{im})] \quad (8b)$$

where A_o = ocean area, and f_i is a typical ratio of column [height-over-flotation:ice thickness] for the ice in question, taken to be ~1000 m/1500 m = 2/3 for ANT marine basins, and 1 for GRN, NAIS, EUR.

Substituting (7) into (5) and re-arranging,

$$V_{om} (\delta_{om} - \delta_o) = -\Sigma[V_{im} (\delta_{im} - \delta_o)] + K \Sigma[V_{il} (\alpha_i + \beta_i \Delta T + \gamma_i V_{im} - \delta_o)]$$
$$+ (1-K) \Sigma[V_{im} (\alpha_i + \beta_i \Delta T + \gamma_i V_{im} - \delta_o)] - K^2 \Sigma[((V_{il} - V_{im})^2) \gamma_i]$$
$$- 2 K \Sigma[(V_{il} - V_{im}) V_{im} \gamma_i] - \Sigma[(V_{im}^2) \gamma_i] \quad (9)$$

This is a quadratic equation in K (with all other terms known) of the form $A K^2 + B K + C = 0$, where (in preliminary form)

$$A = \Sigma[((V_{il} - V_{im})^2) \gamma_i]$$

$$B = -\Sigma[V_{il} (\alpha_i + \beta_i \Delta T + \gamma_i V_{im} - \delta_o)] + \Sigma[V_{im} (\alpha_i + \beta_i \Delta T + \gamma_i V_{im} - \delta_o)] + 2 \Sigma[(V_{il} - V_{im}) V_{im} \gamma_i]$$

$$C = V_{om} (\delta_{om} - \delta_o) + \Sigma[V_{im} (\delta_{im} - \delta_o)] - \Sigma[V_{im} (\alpha_i + \beta_i \Delta T - \delta_o)]$$

These simplify to the final versions for A, B, and C

$$A = \Sigma[((V_{il} - V_{im})^2) \gamma_i]$$

$$B = -\Sigma[(V_{il} - V_{im}) (\alpha_i + \beta_i \Delta T - V_{im} \gamma_i - \delta_o)]$$

$$C = V_{om} (\delta_{om} - \delta_o) - \Sigma[V_{im} \beta_i \Delta T]$$

This final equation for C follows because $\delta_{im} = \alpha_i$ (Eq. 4 applied to modern conditions for which $\Delta T = 0$).

The two solutions are

$$K = \left(-B \pm \sqrt{B^2 - 4AC}\right)/(2A) \quad (10)$$

For colder intervals with ΔT substantially less than 0 and δ_o substantially greater than δ_{om}, it can be seen that $A > 0$, $B > 0$, $C < 0$ always, so the solution with the positive square root ($+\sqrt{}$) will always yield positive real K, as required. Valid solutions with $K > 0$ are also possible for δ_o very close to zero, or $\delta_o > 0$ and $\Delta T > 0$. As noted above, all three quadratic solutions (in subsections 2.1.1 to 2.1.3) were tested for each combination of ΔT and δ_o in our data, always finding at most one valid solution with sea level in the appropriate range.

2.1.2. Equations for generally warmer climates (no NAIS, EUR; smaller than present GRN, ANT; sea level 0 to 14 m above present)

For moderate warming above present, there is no NAIS or EUR. ANT is present, and GRN still exists with SLR assumed to be in the range 0 to 14 m above modern. The same expression as above for mean ice-sheet $\delta^{18}O$ is still used, but only with i = 1 to 2 for ANT and GRN:

$$\delta_i = \alpha_i + \beta \Delta T - \gamma_i (V_i - V_{im})$$

As in the derivation above for colder climates, we still have

$$V_{om} (\delta_{om} - \delta_o) = - \Sigma[V_{im} (\delta_{im} - \delta_o)] + \Sigma[V_i (\alpha_i + \beta_i \Delta T - \gamma_i (V_i - V_{im}) - \delta_o)] \quad (11)$$

In the derivation in subsection 2.1.1, there were four unknowns (V_i, i=1 to 4), and three additional equations were needed (Eq. 6). Here there are only two unknowns (V_i, i=1 to 2), and just one additional equation is needed. We cannot use the "K" form (Eq. 6) because GRN and ANT do not decrease proportionally. Instead, we assume that both ice sheets contribute equal absolute amounts of SLR up to 14 m total, i.e.,

$$(V_i - V_{im}) \text{ for GRN} = (2/3) (V_i - V_{im}) \text{ for ANT}$$

where 2/3 is a typical ratio of column [height-over-flotation:ice thickness] for ANT marine ice grounded below sea level. This can be written as

$$\Delta V = f_i (V_i - V_{im}) \text{ for } i = 1 \text{ and } 2 \quad (12)$$

where ΔV is a single number (independent of ice sheet), and $f_i = 1$ for GRN and 2/3 for ANT. Of course, for consistency this requires that V_{2m} (modern Greenland) = 7 x A_o.

Re-writing (12) as $V_i = \Delta V/f_i + V_{im}$ and substituting into (11) yields

$$V_{om} (\delta_{om} - \delta_o) = - \Sigma[V_{im} (\delta_{im} - \delta_o)] + \Sigma [(\Delta V/f_i + V_{im}) (\alpha_i + \beta_i \Delta T - \gamma_i \Delta V/f_i - \delta_o)] \quad (13)$$

This is a quadratic for ΔV, of the form $A \Delta V^2 + B \Delta V + C = 0$.

Re-arranging and simplifying,

$$A = \Sigma [\gamma_i / (f_i^2)]$$

$$B = - \Sigma [(\alpha_i + \beta_i \Delta T - V_{im} \gamma_i - \delta_o) / f_i]$$

$$C = V_{om} (\delta_{om} - \delta_o) - \Sigma[V_{im} \beta_i \Delta T]$$

The solutions are

$$\Delta V = \left(-B \pm \sqrt{B^2 - 4AC}\right)/(2A) \quad (14)$$

A is always < 0, but the signs of B and C are not readily apparent, and we cannot say *a priori* which sign of the square root (if any) yields a negative real ΔV with $-7 < \Delta V < 0$ so that $0 < SLR < 14$ as required. But if one exists, it is the valid solution for this interval with both GRN and ANT present.

Then $V_i = \Delta V/f_i + V_{im}$, and

$$SLR \times A_o = -\Sigma[f_i (V_i - V_{im})] = -\Sigma[\Delta V] = - 2 \Delta V$$

2.1.3. Equations for much warmer climates (no NAIS, EUR, GRN; sea level > 14 m)

For greater warming with GRN entirely melted, SLR is assumed to be > 14 m, with only a reduced ANT existing. We still need to use equations for i = 1 to 2 involving both GRN and ANT, because 7 m of the > 14 m SLR is from the melted GRN. Starting with Eq. (11), the one additional equation is simply

$V_2 = 0$ (choosing i=1 for Antarctica, i=2 for Greenland).

Then (11) becomes an equation for Antarctic volume V_1:

$$V_{om} (\delta_{om} - \delta_o) = - \Sigma[V_{im} (\delta_{im} - \delta_o)] + V_1 (\alpha_1 + \beta_1 \Delta T - \gamma_1 (V_1 - V_{1m}) - \delta_o)] \quad (15)$$

Again, this is a quadratic for V_1 of the form $A V_1^2 + B V_1 + C = 0$, where

$A = \gamma_1$

$B = - (\alpha_1 + \beta_1 \Delta T + \gamma_1 V_{1m} - \delta_o)$

$C = V_{om} (\delta_{om} - \delta_o) + \Sigma[V_{im} (\delta_{im} - \delta_o)]$

The two solutions are

$$V_1 = \left(-B \pm \sqrt{B^2 - 4AC}\right)/(2A) \quad (16)$$

Always $A < 0$ and $B > 0$, but the sign of C is not apparent, so real solutions may be possible with either sign of the square root. If one is, and it is in the required range $0 < V_1 < V_{1m} - 7 A_o / (2/3)$ so that SLR is > 14 m, then it is the valid solution for this interval with only ANT remaining, and

$$SLR \times A_o = -\Sigma[f_i (V_i - V_{im})] = V_{2m} - (2/3) (V_1 - V_{1m})$$

For SLR up to approximately +25 m, the ANT contribution is nearly all from marine basins. Using $f_1 = 2/3$ as above is thus appropriate, and we do not need to consider ice loss from the terrestrial East AIS.

For a very few of the combinations of mean ocean water $\delta^{18}O_{sw}$ and global surface temperature in our data (32 out of 4883), no valid quadratic solutions were found with any of the three derivations described in subsections 2.1.1 to 2.1.3 above. These all occur in the Pliocene, and the neighboring timesteps in the data all yield SLR close to +14 m. This is probably because the physical assumptions at the border of our two "warmer" scenarios in sections 5.2 and 5.3 are too restrictive, i.e., Greenland vanishing precisely at SLR = 14 m with exactly the same SLR

contribution as Antarctica at that point. We suspect that if these assumptions were loosened slightly, these 32 combinations would yield valid solutions with SLR close to +14 m.

2.2. Estimating α_i, β_i, and γ_i values

In all colder and warmer climate cases, we use a simple expression for mean ice sheet $\delta^{18}O_i$ (δ_i), linearized about the modern state for ANT and GRN, or about the nascent (first-formed) ice caps for NAIS and EUR (α_i):

$$\delta_i = \alpha_i + \beta_i \Delta T - \gamma_i (V_i - V_{im})$$

β_i describes how δ_i responds to changes in global temperature at fixed ice-sheet size (via changes in $\delta^{18}O$ of precipitation, $\delta^{18}O_{precip}$, i.e., a Dansgaard-like coefficient), and γ_i describes how δ_i responds to changes in ice-sheet size at fixed global temperature. The values of the coefficients α_i, β_i and γ_i are obtained mostly from results of published GCM and ice-sheet model experiments (*22, 25-27*), as described below.

For GRN and ANT, α_i is the modern ice-sheet mean $\delta^{18}O$, i.e., $\alpha_i = \delta_{im}$.

α_{GRN} = -34 ‰ (*25*)

For ANT, we combine values for the West and East Antarctic ice sheets (*25*), weighted by their modern volumes:

V_{im} of WAIS = 5 m (sea-level equivalent) (*25*)

δ_{im} of WAIS = -41 ‰ (*25*)

V_{im} of EAIS = 47.5 m (sea-level equivalent) (*25*)

δ_{im} of EAIS = -56.5 ‰ (*25*)

α_{ANT} = (5*(-41) + 47.5*(-56.5)) / (5+47.5) = -55 ‰

For NAIS and EUR, α_i is the $\delta^{18}O_{precip}$ of the nascent (first-formed) ice cap for each ice sheet. We use values tuned to fit the 130 m sea-level lowstand at the LGM.

A_{NAIS} = -14 ‰

α_{EUR} assumed same as NAIS = -14 ‰

β_i coefficients are estimated from GCM experiments in (*27*) where the ice-sheet size is fixed (at modern, or with the virtual extent fixed for NAIS, EUR) and climate is changed (labelled PI and $SST_{(LGM)}$ in (*27*). The change in mean $\delta^{18}O_{precip}$ in these experiments is assumed equal to the change in δ_i that would result after the ice has infinite time to advect internally and equilibrate to the permanent change in climate. β_i is thus estimated from such GCM experiments as:

$\beta_i = \Delta\delta^{18}O_{precip} / \Delta T$

The fixed ice size in these experiments is of course artificial; an actual ice sheet would grow or retreat due to the change in surface mass balance, but this is purposely excluded in estimating β_i.

Case 1: β_i and γ_i for colder climates than present:

Using results of the $SST_{(LGM)}$ experiment vs. modern (with fixed ice) from *Tharammal et al.* (*27*):

B_{NAIS} = -1.5 ‰ / -2.79 °C = 0.54 ‰/°C

β_{EUR} = -2.77 ‰ / -2.79 °C = 1 ‰/°C

β_{GRN} = -2.6 ‰ / -2.79 °C = 0.93 ‰/°C

β_{ANT} = -1.24 ‰ / -2.79 °C = 0.44 ‰/°C

γ_i is the coefficient describing how δ_i responds to changes in ice-sheet size at fixed global temperature. It is estimated using modeled changes in δ_i for LGM vs. modern, after subtracting the component of δ_i change due to temperature (i.e., $\beta_i \Delta T$). Subtracting the δ_i equations for modern and LGM:

$\gamma_i = - [(\delta_{il} - \delta_{im}) - \beta_i \Delta T_{lgm}] / (V_{il} - V_{im})$

For NAIS, $\delta_{il} - \delta_{im}$ = -7 ‰ (*26*)

For EUR, assume $\delta_{il} - \delta_{im}$ = NAIS value = -7 ‰

For GRN, $\delta_{il} - \delta_{im}$ = -3 ‰ (*25*)

For ANT, δ_{im} = -55 ‰ (as calculated above from (*25*)

For ANT δ_{il}, we combine separate values for West and East Antarctic ice sheets (WAIS, EAIS, respectively) for the LGM, from (*25*):

V_{il} of WAIS = 24.6 m (sea-level equivalent)

δ_{il} of WAIS = -42.5 ‰ (*25*)

V_{il} of EAIS = 52 m (sea-level equivalent)

δ_{il} of EAIS = -56.5 ‰ (*25*)

δ_{il} = (24.6 x(-42.5) + 52 x(-56.5)) / (24.6+52) = -52 ‰, so

$\delta_{il} - \delta_{im}$ = +3 ‰

ΔT_I = -6°C (LGM global temperature anomaly from (*28*)), so:

$\gamma_{NAIS} = - [-7 - 0.54x(-6)] / (88 \times A_o) = 1.181 \times 10^{-16}$ ‰/m^3

$\gamma_{EUR} = - [-7 - 1.0x(-6)] / (24.5 \times A_o) = 1.13 \times 10^{-16}$ ‰/m^3

$\gamma_{GRN} = - [-3 - 0.93x(-6)] / (3.1 \times A_o) = -2.30 \times 10^{-15}$ ‰/m^3

$\gamma_{ANT} = - [+3 - 0.44x(-6)] / (21.6 \times A_o) = -7.23 \times 10^{-16}$ ‰/m^3

For NAIS and EUR, γ_i is positive, reflecting the lighter $\delta^{18}O_{precip}$ on the higher ice sheet plateaus at maximum LGM size, compared to on the lower initial nascent ice patches. For GRN and ANT, γ_i is negative, because ice sheet expansion from modern mainly involves additional marginal marine ice growth at low elevations with heavier $\delta^{18}O$, compared to the existing interior ice with lighter $\delta^{18}O$.

Case 2: β_i and γ_i for warmer climates than present (ANT and GRN only):

For ANT, we assume that β_i estimated from (*27*) above for colder climates still holds for warmer climates. It measures how $\delta^{18}O_{precip}$ changes at fixed ice-sheet size, and presumably that is similar for positive and negative ΔT.

So, $\beta_{ANT} = 0.44$ ‰/°C

For γ_{ANT}, similarly to above, subtracting the δ_i equations for the modern (m) and Pliocene (p):

$$\gamma_i = - [(\delta_{ip} - \delta_{im}) - \beta_i (\Delta T_p)] / (V_{ip} - V_{im})$$

From Table 1 in (*22*), referencing the simulation of (*29*), $\beta_i \Delta T_p = 7.5$ ‰, $\delta_{ip} - \delta_{im} = 3.8$ ‰, and $V_{ip} - V_{im} = -11.3$ m sea-level equivalent, so that

$$\gamma_{ANT} = - [3.8 - 7.5] / (-11.3 \times A_o) = -9.05 \times 10^{-16} \text{ ‰/m}^3$$

This agrees quite closely with γ_{ANT} derived above for colder climates; both are negative, representing changes in low-elevation marine ice with $\delta^{18}O \sim -40$ ‰, while terrestrial (mostly EAIS) ice remains ~constant with $\delta^{18}O \sim -55$ ‰. This is valid for warmer climates only up to SLR ~ + 25 m, when essentially all ANT marine basins have retreated. Beyond that, EAIS terrestrial ice would retreat back to the nascent point, and γ_i would be positive, but this situation is not applicable to the past 4.5 Myr.

For GRN, we use the same $\beta_i = 0.93$ as for colder climates above, but a different γ_i, because unlike Antarctica, retreat from modern is mostly into terrestrial ice, not marine. Since no retreated-Greenland isotopic model simulations are available to our knowledge, we assume the same γ_i as for EUR in cold climates above:

$$\gamma_{GRN} = 1.35 \times 10^{-16} \text{ ‰/m}^3$$

2.3. Time averaging ΔT based on ice residence time

965 The β_i ΔT term in the equation for δ_i above is for equilibrated changes, i.e., after the ice
966 has infinite time to respond to a permanent change in climate and $\delta^{18}O_{precip}$. However, in a real ice
967 sheet $\Delta\delta^{18}O_i$ records $\Delta\delta^{18}O_{precip}$ over a past interval on the order of the mean residence time of ice
968 within the ice sheet. To crudely account for this, the δ_i equation for the time-evolving ice sheets is
969 modified to:

970 $$\delta_i = \alpha_i + \beta_i \, INT[\Delta T] - \gamma_i \, (V_i - V_{im})$$

971 where INT[ΔT] is the time average of ΔT from t-τ' to t, t is the current time, and τ' is the minimum
972 of the average ice age (τ_i) and how long ago the ice sheet last vanished ($V_i = 0$), because if the ice
973 sheet vanishes, its ice-$\delta^{18}O$ memory is wiped out. Then all occurrences of ΔT are replaced by
974 INT[ΔT] in Eqs. (5), (9), and the equations for the quadratic coefficients B and C in all cases
975 above.

976 For GRN and ANT, mean residence times are obtained directly from (*25*), averaging their
977 West and East Antarctic values together for ANT in the ratio 5:50:

978 $$\tau_{ANT} = (5 \times 44 + 50 \times 125)/55 = 118 \text{ kyr}$$

979 $$\tau_{GRN} = 41 \text{ kyr}$$

980 For NAIS, we assume that the average residence time is on the order of one glacial cycle:

981 $$\tau_{NAIS} = 100 \text{ kyr}$$

982 For EIS, it is assumed to be roughly midway between GRN and NAIS:

983 $$\tau_{EIS} = 60 \text{ kyr}$$

984 We note that τ = 41 kyr should be used for the 41-kyr world (pre-MPT), but this issue is
985 partially accounted for by using τ' as the minimum of the nominal value and the interval from the
986 last time the ice sheet vanished ($V_i = 0$) to the current time. τ' thus will not be longer than 41 kyr

if $V_i(t)$ is decreasing to zero realistically as it should in the 41-kyr world. This "minimum" correction reduces the nominal τ values for the 41-kyr world.

2.4. List of prescribed quantities

V_{om} = modern ocean volume = 1.35 x 10^{18} m^3

A_o = ocean area = 3.62 x 10^{14} m^2

δ_{om} = modern ocean $\delta^{18}O$ = 0 ‰

V_{im} = modern volume of ice sheet i (liquid equivalent) = sea level change x A_o:

NAIS = 0 m x A_o = 0 m^3

EIS = 0 m x A_o = 0 m^3

GRN = 6.7 m x A_o = 2.47 x 10^{15} m^3

WAIS = 5 m x A_o = 1.81 x 10^{15} m^3

EAIS = 47.5 m x A_o = 1.72 x 10^{16} m^3

ANT = WAIS + EAIS = 52.5 m x A_o = 1.94 x10^{16} m^3

V_{il} = LGM volume of ice sheet i (liquid equivalent) = sea level equivalent x A_o:

NAIS = 88 m x A_o = 3.19 x 10^{16} m^3 (*30*)

EIS = 24.5 m x A_o = 8.87 x 10^{15} m^3 (modified from 23.5 m in (*30*))

GRN = 3.1 m (LGM excess) x A_o = 1.12 x 10^{15} (LGM excess) + 2.47 x 10^{15} (modern)

= 3.59 x 10^{15} m^3

WAIS = 19.6 m (LGM excess) x A_o = 7.10 x 10^{15} m^3

EAIS = 2 m (LGM excess) x A_o = 7.24 x 10^{14} m^3

ANT = WAIS + EAIS = 21.6 m (LGM excess), of which 2/3 (14.4 m) contributes to sea level

ANT = 7.82 x 10^{15} m^3 (LGM excess) + 1.94 x 10^{16} m^3 (modern) = 2.72 x 10^{16} m^3

Total LGM sea-level fall = 88+24.5+3.1+14.4 = 130 m

1010 δ_{im} = modern $\delta^{18}O$ of ice sheet i:

1011 NAIS = -14 ‰

1012 EIS = -14 ‰

1013 GRN = -34 ‰ (*25*)

1014 WAIS = -41 ‰ (*25*)

1015 EAIS = -56.5 ‰ (*25*)

1016 ANT = WAIS + EAIS = [5x(-41) + 47.5x(-56.5)] / [5+47.5] = -55 ‰

1017 δ_{il} = LGM $\delta^{18}O$ of ice sheet i:

1018 NAIS = -21 ‰

1019 EIS = -21 ‰

1020 GRN = -37 ‰ (*25*)

1021 WAIS = -42.5 ‰ (*25*)

1022 EAIS = -56.5 ‰ (*25*)

1023 ANT = WAIS + EAIS = [24.6*(-42.5) + 52*(-56.5)] / [24.6+52] = -52 ‰

1024

1025

1026 ***2.5. Sea-level reconstruction sensitivity tests***

1027 The dependence of $\delta^{18}O_{ice}$ on ice elevation and temperature may have differed further back
1028 in time due to changes in ice-sheet geometry, temperature gradients, and accumulation seasonality.
1029 We thus conducted several sensitivity tests to explore the robustness of our sea-level reconstruction
1030 to these dependencies. We first altered the β_i values in our model by a factor of two higher and
1031 lower, adjusting α_i and γ_i values to be consistent with these perturbed β_i values and the LGM ice-
1032 sheet volume and $\delta^{18}O$ changes used in our standard scenario. These changes in β_i mostly affect

the magnitude of sea-level lowstands during early Pleistocene glaciations, in particular deepening them with larger β_i values because this yields heavier $\delta^{18}O_i$ due to warmer temperatures (fig. S4A). We next found that 1σ uncertainties of 0.2 to 0.6°C in our ΔMOT reconstruction used to derive $\delta^{18}O_{sw}$ (*9*) translate to $\delta^{18}O_{sw}$ uncertainties of ~0.05 to 0.15 ‰ and corresponding sea-level uncertainties of ~5 to 25 m (fig. S4B). These uncertainties are typically larger in the late Pleistocene due to the higher MOT:SST scaling then, as well as in the Pliocene due to the smaller number of SST records used to derive MOT (*9*).

Lastly, we evaluated how much an underestimation of MOT glacial-interglacial variability prior to the MPT might affect reconstructed sea levels by recalculating sea levels after amplifying the power in the orbital bands (15-25 and 35-45 kyr) in our ΔMOT reconstruction (*9*) prior to 1 Ma by factors of five and ten. The resulting sea-level reconstructions show that sea-level lowstands during the early Pleistocene remained below -100 m regardless of the scenario (fig. S4C). Although these sensitivity analyses reveal how various details of our GMSL reconstruction could be altered by future work, they suggest that our finding of LGM-like sea-level lowstands during the early Pleistocene is robust across a wide range of parameter values in our model and is consistent with several lines of geological evidence.

3. Time series analyses

We characterized the temporal variability and covariability of the different time series in four ways, using: 1) evolutionary spectra (Fig. 2A); 2) "global" multitaper spectral analysis (Fig. 2B); 3) bandpass-filtered time series of ΔGMST and SL at the 41 kyr obliquity period (Fig. 2C); and 4) the rolling coherence between the filtered series and obliquity (Fig. 2D). Evolutionary spectra (*31*) were calculated using the R astrochron package (*32, 33*). The function eha() in the astrochron package implements a moving-window application of the multi-taper method (MTM)

spectral-analysis procedure (*34*). We used a window width of 500 kyr, a time step of 10 kyr between adjacent window positions, and a "standard" MTM time-bandwidth product of 4. Prior to analysis, the time series were detrended using a smoothing spline with 10 degrees of freedom using the spline.smooth() function in the R base stats package (*33*). This detrending step removes the very long-period variability from the time series but does not obscure or overly emphasize the eccentricity band variations in the data. The spectral density was rescaled to "normalized amplitude" values—in each window, the amplitudes (the square root of the spectral density) at each frequency were divided by the maximum amplitude across all frequencies. This facilitates judging the relative importance of variations across periods. We did not do any significance testing of the results because the presence of variability in the time series at orbital frequencies is really not in question, and white-noise or low-order autoregressive null-hypothesis spectra are rather naïve. On Fig. 2A, the dominant periods in insolation variations at orbital periods are indicated by horizontal lines (eccentricity: E_1 = 400 kyr, E_2 = 96 kyr; obliquity: T = 41 kyr and precession: P_1 = 23 kyr, P_2 = 19 kyr).

Global (as opposed to evolutionary) spectral analysis was performed for blocks of data, as indicated by the black horizontal bars on Fig. 2A. We used the multitaper method here as well. We bandpass-filtered the time series at the 41 kyr obliquity period using the butter() (Butterworth filter) function from the R signal package (*35*). The band limits were 39.0 and 43.1 kyr, 0.95 and 1.05 times the obliquity frequency of 1/41.0 = 0.0244 cycles kyr^{-1}. The coherence between obliquity and ΔGMST and SL was calculated using a moving window approach. Cross-spectral analyses were done following the Blackman-Tukey method using the SPECTX2 function from the ARAND software package (*36*). The number of lags used correspond to ~1/3 the length of the interval analyzed.

4. Ice-sheet surface mass balance

We assessed the sensitivity of the surface mass balance (SMB) of early Pleistocene Northern Hemisphere ice sheets to orbits, atmospheric CO_2, and ice-sheet height by conducting experiments with the GENESIS V3.0 climate model (*37, 38*) (Table S1). The GENESIS climate model comprises a T31 atmospheric model (horizontal resolution of approximately 3.75° × 3.75° latitude by longitude) coupled with the land-surface model LSX (2° × 2° resolution). SSTs were computed by the 50-meter mixed layer ocean model in GENESIS. SMB is computed from annual precipitation, runoff, and evaporation over the ice sheets on the 2° ×2° grid of the LSX land surface model. The fraction of runoff retained through refreezing is computed as a function of temperature and precipitation using the method of Ref. (*39*). We ran the simulations for 100 years and analyzed the last 70 years to exclude spin-up artifacts.

Our sensitivity experiments used orbits corresponding to low (glacial) and high (interglacial) obliquity at 2.165 Ma and 2.145 Ma (*40*), respectively, and atmospheric CO_2 values of 200 and 300 ppmv which cover much of the early Pleistocene range suggested by proxies (*41-43*). We used three ice-sheet configurations to assess sensitivity to ice-sheet height for a given LGM area (Table S1). The GLAC-1D LGM ice sheets are from Ref. (*44*). The HIGH ice sheets are intended to represent the largest of the early Pleistocene ice sheets, with ~30 m of additional lowering of sea-level relative to the LGM sea-level lowstand (Figs. 1C, 3E). We derived the HIGH ice-sheet heights by calculating the volume of 30 m of global sea level and distributing the height equivalent of the volume uniformly over the GLAC 1-D LGM North American (NA) (20 m) and Eurasian (EU) (10 m) ice-sheet complexes, accounting for the density ratio of water to ice (1028 kg m^{-3}/910 kg m^{-3}). The LOW ice sheet was derived by reducing the GLAC 1-D LGM ice-sheet

height to an equivalent of 60% of the full LGM sea-level volume and is intended to represent the low-aspect ratio ice-sheet geometry inferred from the regolith hypothesis (*45*).

Experiment EXP1 shows the model's ability to simulate NH (GLAC-1D) ice sheets that are in SMB or have positive SMB under LGM boundary conditions (Table S1). Experiments EXP2 and EXP3 assess the effect of orbital changes on NH ice-sheet SMB (Table S1). In both experiments, NH MATs north of 40°N are 8 K to 9 K colder than the PI due to the presence of the ice sheets while North Atlantic SSTs are 3 K to >5 K colder due to advection of cold air off the NA ice-sheet complex and southward expansion of sea ice (fig. S10A). Warming of the oceans elsewhere partially offsets the NH cooling such that global SSTs are the same as PI and global MATs are 2 K colder than PI (Table S1). The net effect of the boundary conditions yields a glacial NA ice-sheet-complex SMB of 5 m yr^{-1} (fig. S10B) and an interglacial SMB of -11 m yr^{-1}. Comparison of the NA and EU ice-sheet-complex SMB in EXP2 to that of EXP3 indicates that glacial-interglacial obliquity accounts for 16 m yr^{-1} over NA and 2 m yr^{-1} over EU (Table S1, fig. S10C).

Experiments EXP2 and EXP4 assess the effect of CO_2 changes on NH ice-sheet SMB. Over the 200 to 300 ppm range evaluated here, CO_2 accounts for 15 m yr^{-1} in the NA ice-sheet complex SMB and 8 m yr^{-1} in the EU ice-sheet complex SMB, which are comparable to the effect of obliquity (Table S1). Experiments EXP2 and EXP5 and experiments EXP4 and EXP6 assess the effect of ice-sheet height on NH ice-sheet SMB (Table S1). Lowering the ice-sheet height from HIGH (EXP2) to GLAC-1D (EXP5) results in SMB becoming more negative by 35 m yr^{-1} for the NA ice-sheet complex and 11 m yr^{-1} for the EU ice-sheet complex (Table S1). The effect of height on mass balance is most evident along the margin of the NA ice-sheet complex (fig. S10D) where the higher margin blocks penetration of precipitation into the interior (orographic shadowing) and

positions more ice area at or above the zero-degree isotherm. The marginally more positive SMB over the interior of the NA ice-sheet complex for the lower ice sheet where precipitation is slightly greater than that of the high ice sheet reflects the effect of desertification.

Lowering the ice sheet from HIGH (EXP4) to LOW (EXP6) results in SMB becoming more negative by 84 m yr^{-1} for the NA ice-sheet complex and by 4 m yr^{-1} for the EU ice-sheet complex (Table S1). We note that the strongly negative SMB of the LOW ice sheet in EXP6 (Table S1) indicates that such an ice sheet could not have existed even under glacial orbitals and LGM CO_2 levels.

In summary, our sensitivity tests suggest that early Pleistocene ice sheets that were larger than LGM ice sheets could have been in SMB with low obliquity and CO_2 levels of 300 ppm. SMB becomes more negative as ice-sheet height decreases towards LGM values unless there is a compensatory decrease in CO_2, but no decrease in CO_2 within the range of our current understanding of its Pleistocene variability could support the low-aspect-ratio ice sheets in SMB inferred by the regolith hypothesis (*45*). We note that while our experiments using LSX and a mixed layer ocean model are a first-order assessment of the sensitivity of ice-sheet SMB to changes in boundary conditions, the model does not account for feedbacks such as changes in global ocean circulation and ice-sheet dynamics that, when investigated with a full Earth System model, would further refine our results. The challenge remains for modeling the inception and growth of the ice sheets.

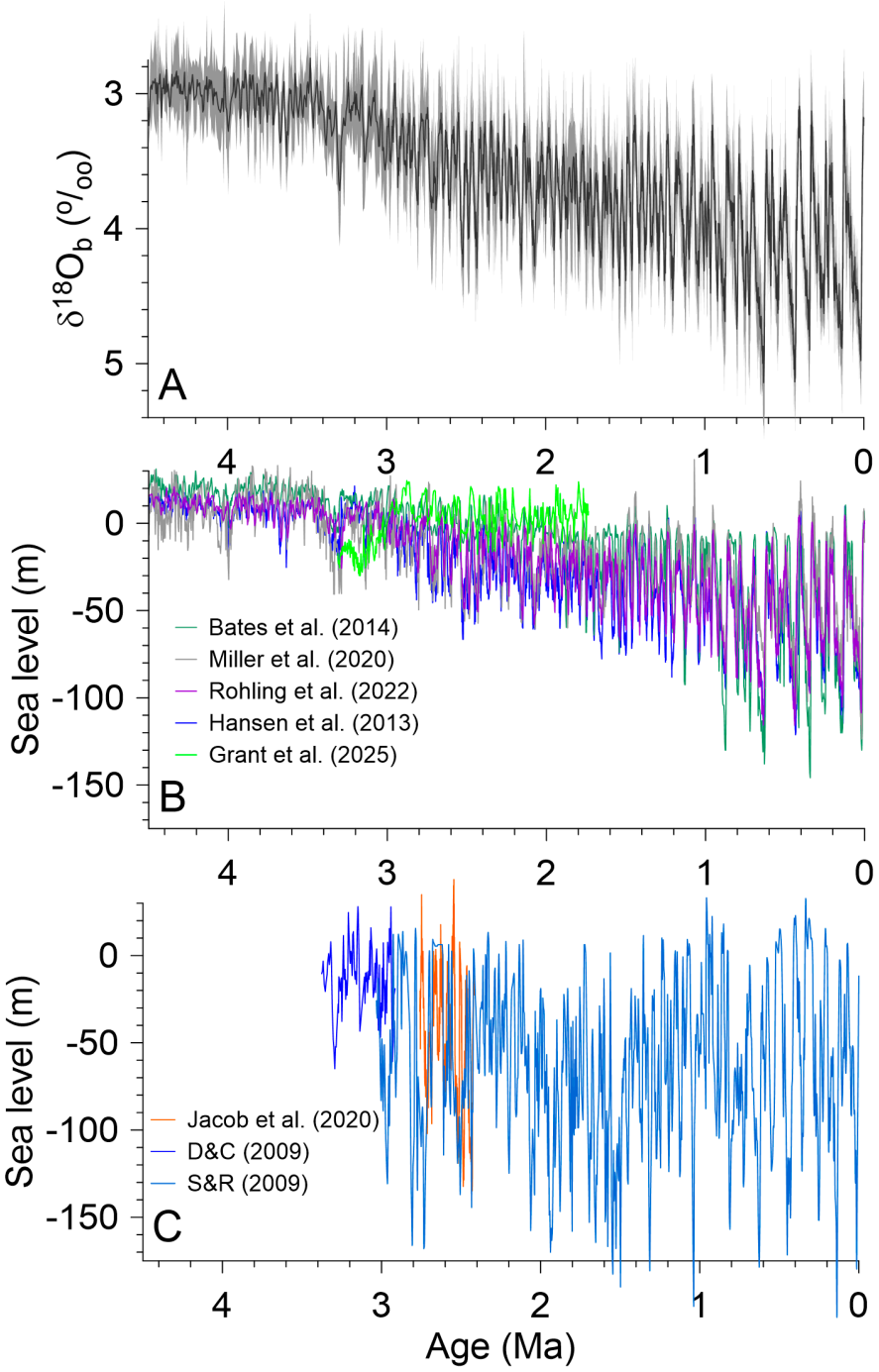

Figure S1. (**A**) Benthic $\delta^{18}O$ stack with 1σ uncertainty (*46*). (**B**) Reconstructions of global sea level. Blue line from Ref. (*7*), light green line from Ref. (*3*), purple line from Ref. (*4*), dark gray line from Ref. (*15*), dark green line from Refs. (*20, 21*). (**C**) Reconstructions of global sea level. Orange line from Ref. (*18*). Dark blue line from Ref. (*17*). Light blue line is based on converting the $\delta^{18}O_{sw}$ data from Ref. (*11*) to sea level using our methodology.

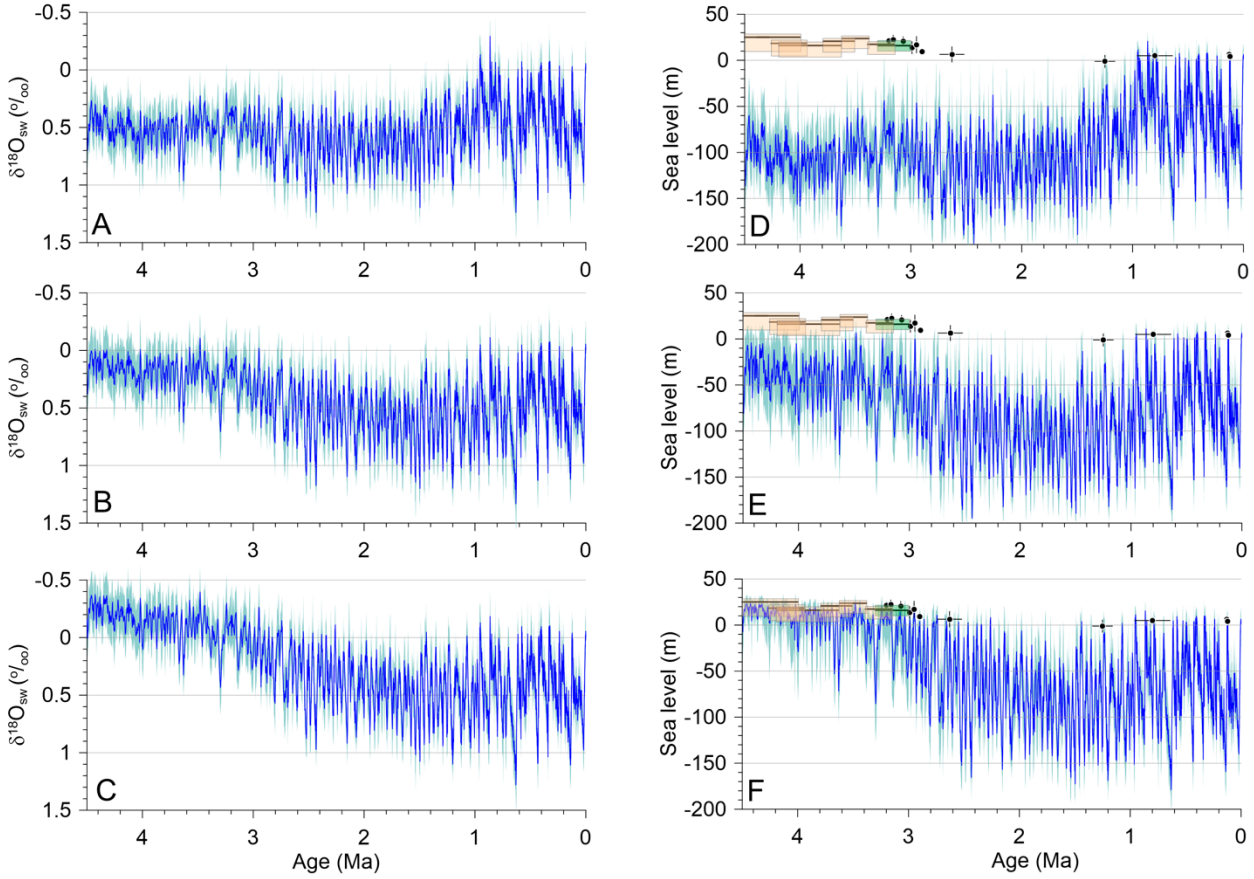

Figure S2. (**A**) Reconstructed $\delta^{18}O$ of seawater ($\delta^{18}O_{sw}$) (1σ uncertainty) based on ΔMOT:ΔSST = 1 (*9*). (**B**) Reconstructed $\delta^{18}O_{sw}$ (1σ uncertainty) based on ΔMOT:ΔSST = 0.5 before 1.5 Ma (*9*). (**C**) Reconstructed $\delta^{18}O_{sw}$ (1σ uncertainty) based on ΔMOT:ΔSST = 0.5 before 1.5 Ma and removal of long-term trend of 0.083‰ Myr^{-1} (*9*). (**D**) Reconstructed sea level (1σ uncertainty) based on $\delta^{18}O_{sw}$ reconstruction in (**A**). Also shown are published Pliocene (*47-49*) and Pleistocene (*50, 51*) sea-level highstands. (**E**) Reconstructed sea level (1σ uncertainty) based on $\delta^{18}O_{sw}$ reconstruction in (**B**). Also shown are published Pliocene (*47-49*) and Pleistocene (*50, 51*) sea-level highstands. (**F**) Reconstructed sea level (1σ uncertainty) based on $\delta^{18}O_{sw}$ reconstruction in (**C**), which is our final reconstruction shown in Fig. 1C. Also shown are published Pliocene (*47-49*) and Pleistocene (*50, 51*) sea-level highstands.

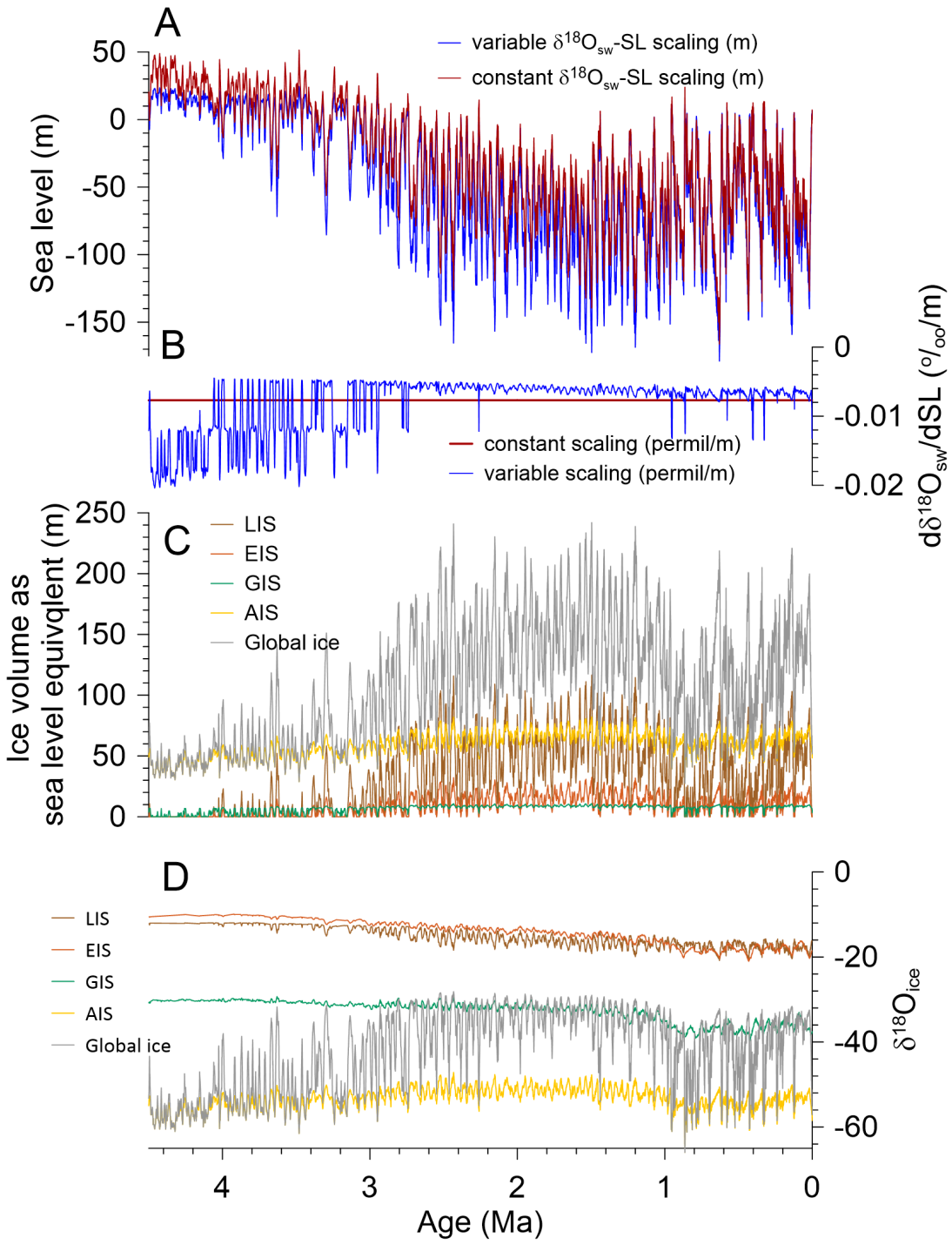

Figure S3. (**A**) Our standard sea-level reconstruction based on variable $\delta^{18}O_{sw}$-sea level scaling (dark blue) compared to using a constant scaling of -0.08‰ m^{-1} (red). (**B**) The $\delta^{18}O_{sw}$-sea level scalings for the sea-level reconstructions shown in panel A. (**C**) Sea-level equivalent ice volumes from our standard reconstruction. (**D**) Ice-sheet mean $\delta^{18}O$ compositions from our standard reconstruction.

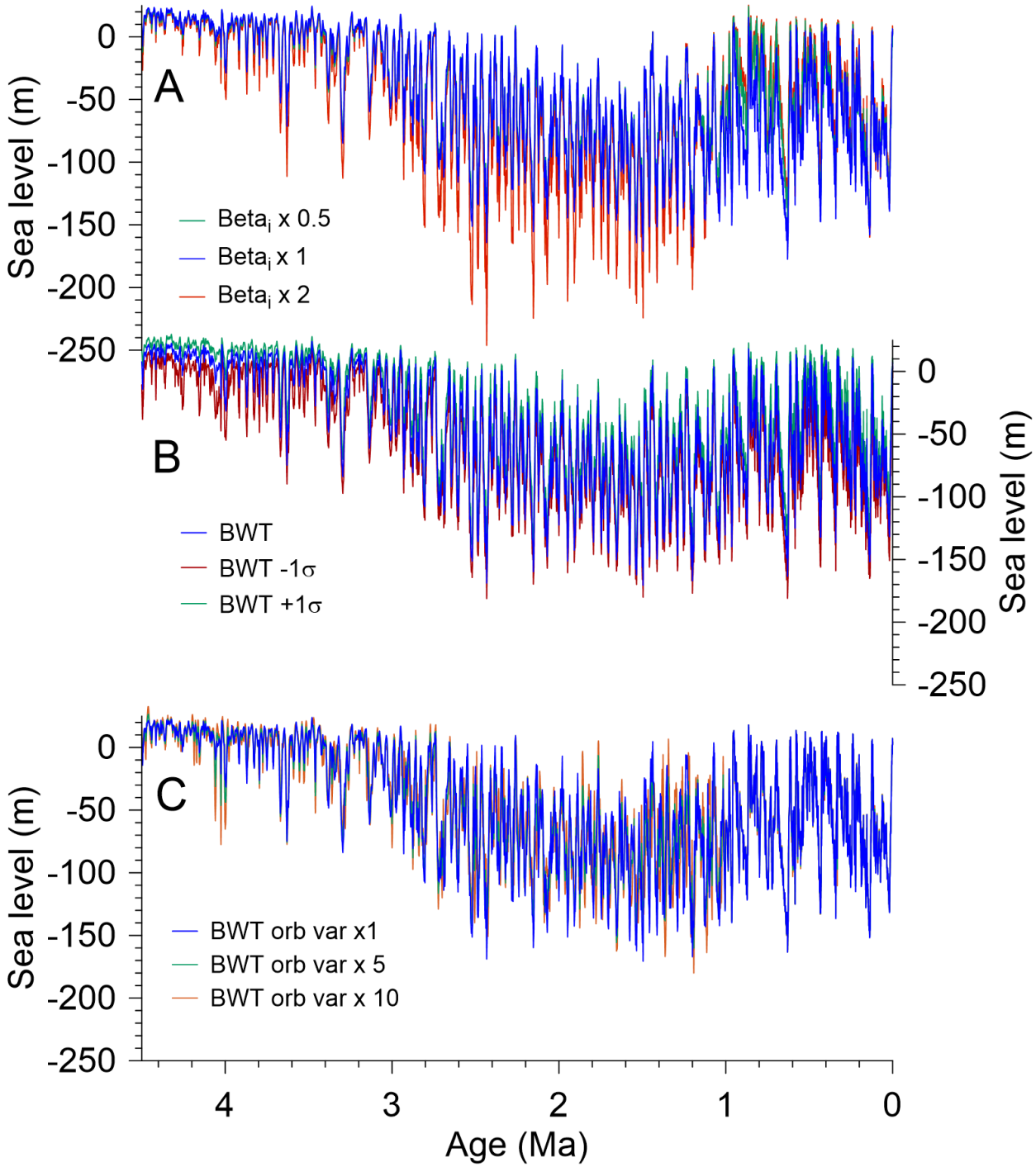

Figure S4. (**A**) Reconstructed sea level using our standard β_i values (blue) compared to β_i values that are half (green) and twice (red) as large. (**B**) Reconstructed sea level using our standard BWT reconstruction (blue) and its lower (red) and upper (green) 1σ range. (**C**) Reconstructed sea level using our standard BWT reconstruction (blue) and reconstructions in which <100-kyr BWT

variability has amplified only the power in the orbital bands (15-25 and 35-45 kyr) by a factor of five (green) and 10 (red).

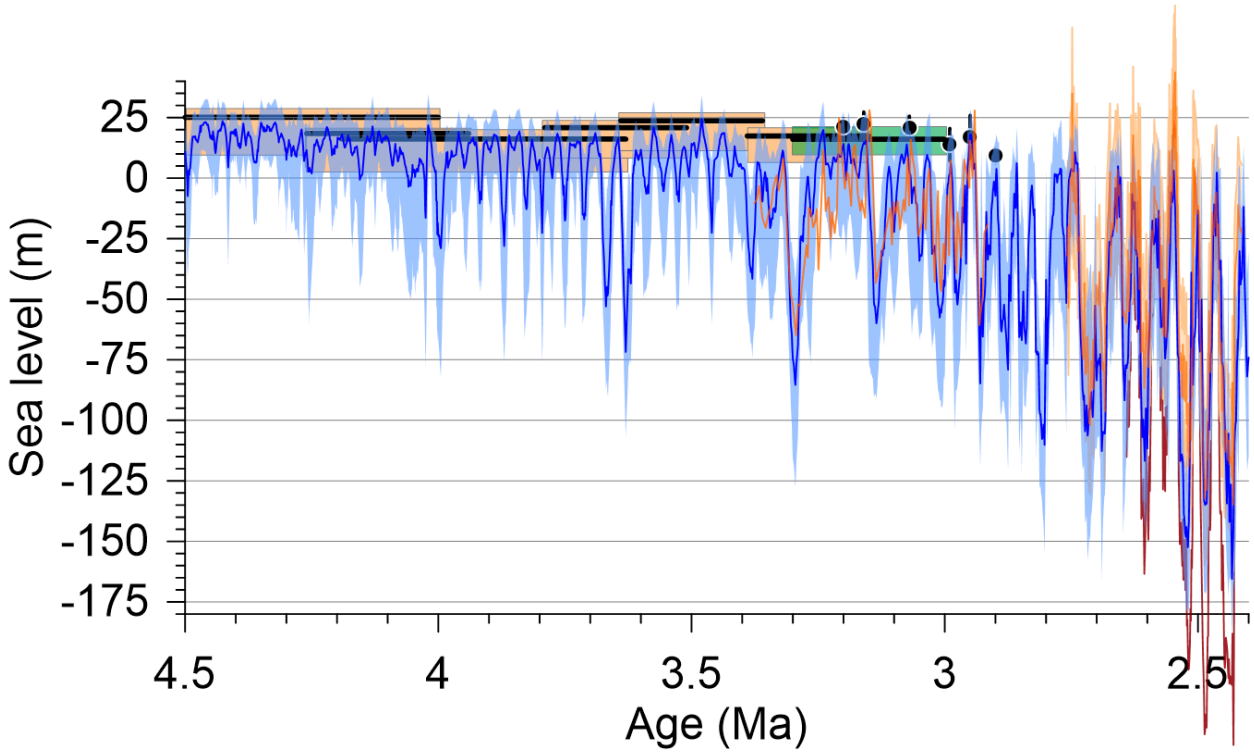

Figure S5. Our sea-level reconstruction during the middle-to-late Pliocene (blue, 1σ uncertainty) compared with sea-level reconstructions from Mallorcan speleothem data (black lines = sea-level mode and age uncertainty, height of orange boxes = 16th and 84th percentile uncertainties) (*48*), Australian coral data (*49*), published sea-level reconstructions based on $\delta^{18}O_{sw}$ reconstructions from ODP site 607 (*17*) and site U1313 (2.4-2.75 Ma) (*18*) (orange lines), with our a sea-level reconstruction for site U1313 based on our methodology, and reconstructions of sea-level high stands from proxy data (black circles) (*47*).

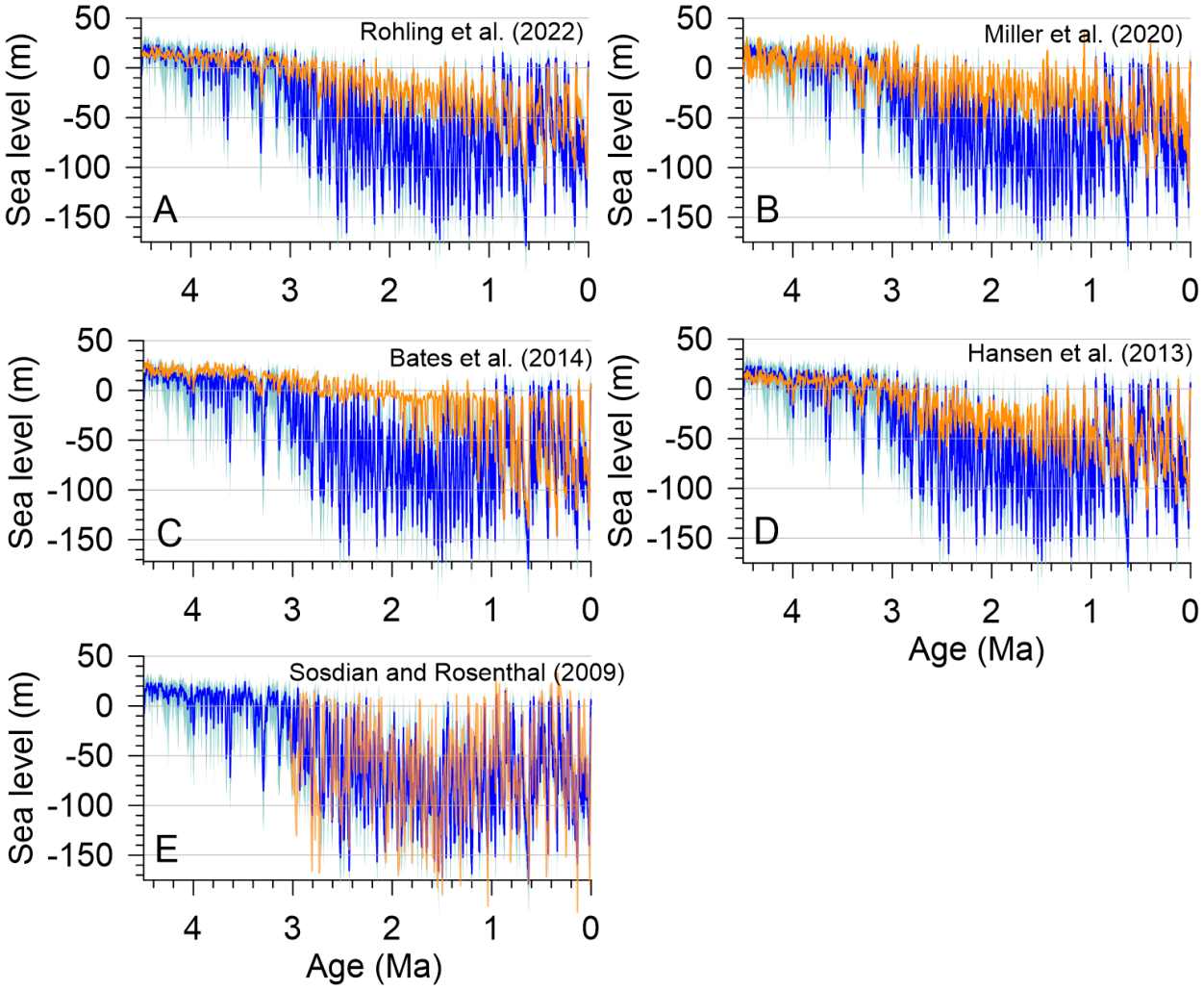

Figure S6. Comparison of our sea-level reconstruction (blue, 1σ uncertainty) to published reconstructions (orange) for last 4.5 Ma. (**A**) Sea-level reconstruction from Ref. (*5*). (**B**) Sea-level reconstruction from Ref. (*15*) (**C**) Sea-level reconstruction from Ref. (*3*). (**D**) Sea-level reconstruction from Ref. (*7*). (**E**) Sea-level reconstruction based on converting the $\delta^{18}O_{sw}$ data from Ref. (*11*) to sea level using our methodology.

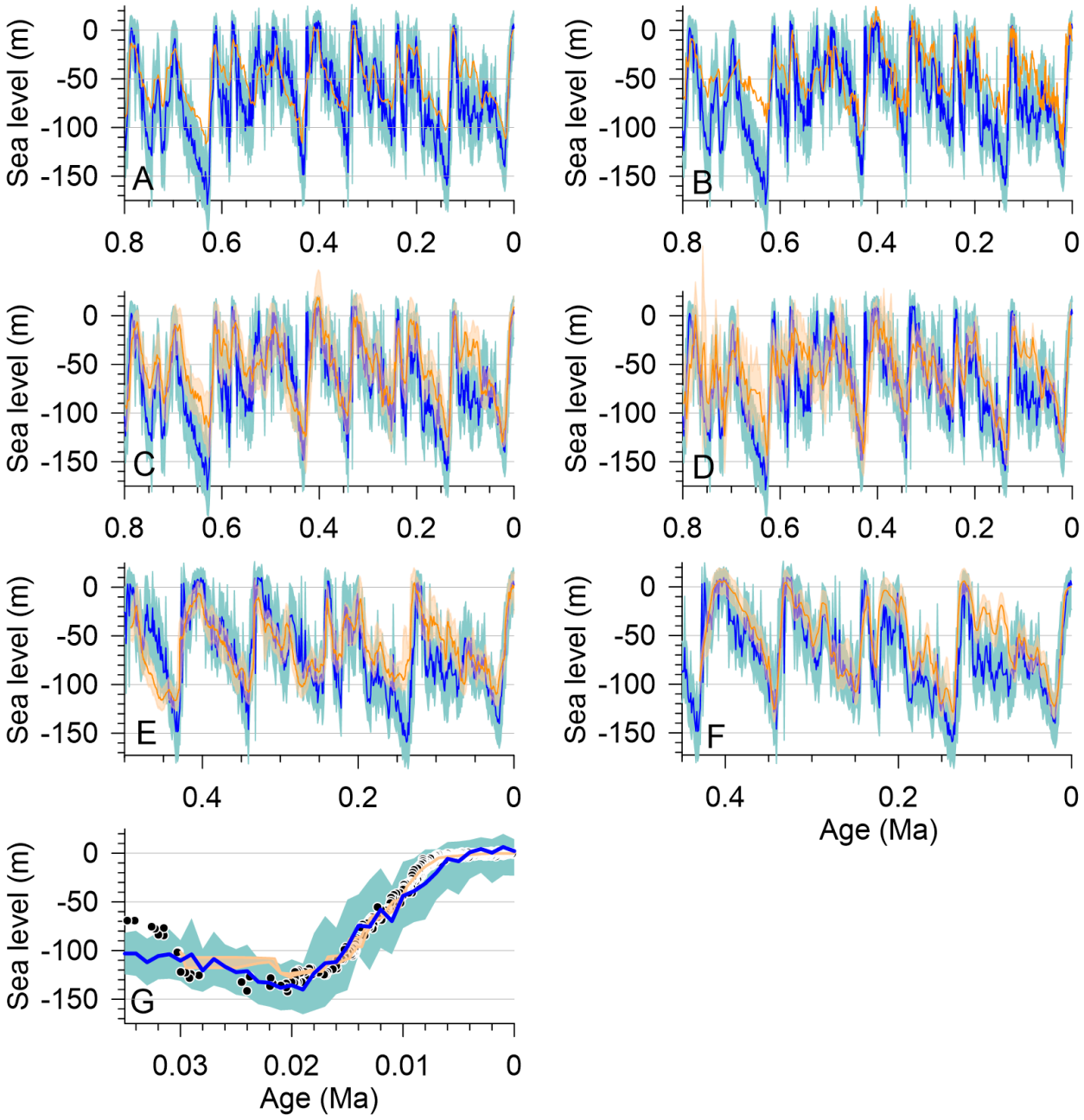

Figure S7. (Comparison of our sea-level reconstruction (blue, 1σ uncertainty) to published reconstructions (orange) for <0.8 Ma. (**A**) Sea-level reconstruction from Ref. (*5*). (**B**) Sea-level reconstruction from Ref. (*15*). (**C**) Sea-level reconstruction from Ref. (*6*). (**D**) Sea-level reconstruction from Ref. (*10*). (**E**) Sea-level reconstruction from Ref. (*52*). (**F**) Sea-level

reconstruction from Ref. (*1*). (**F**) Sea-level reconstruction from Ref. (*24*) (black circles) and Ref. (*53*) (orange, 1σ uncertainty).

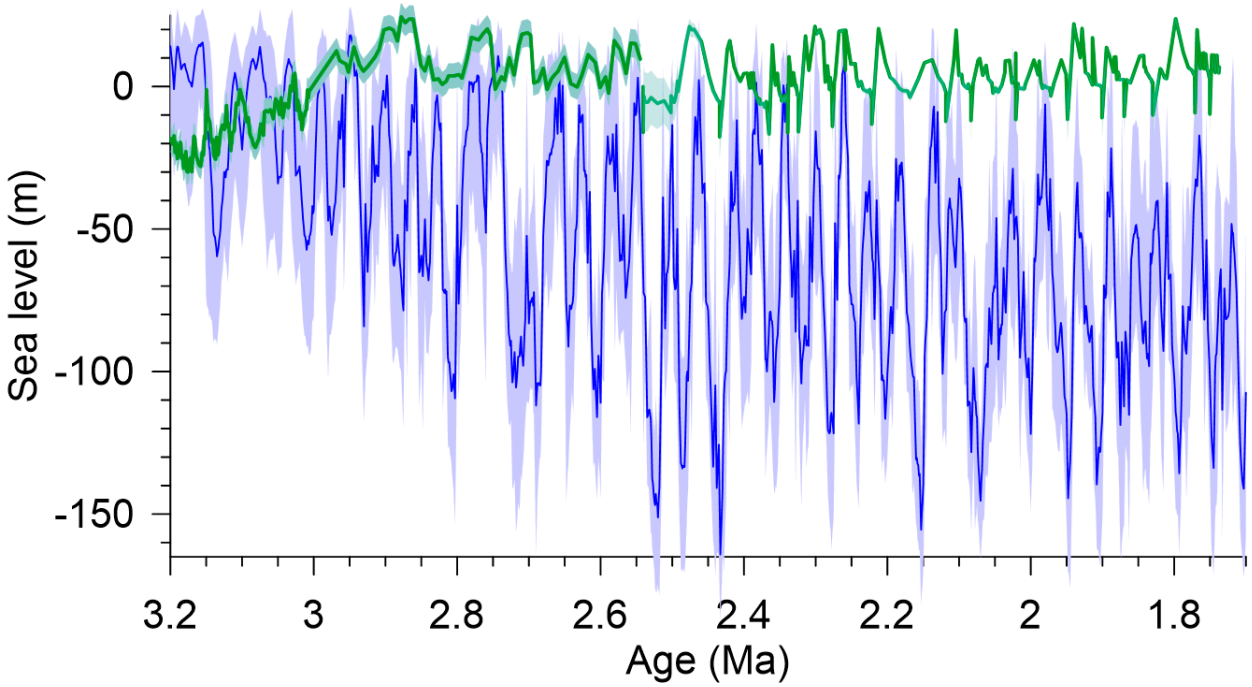

Figure S8. Comparison of our sea-level reconstruction (blue, 1σ uncertainty) to reconstruction from sediments in New Zealand (*20, 21*) (green) for 1.7-3.2 Ma.

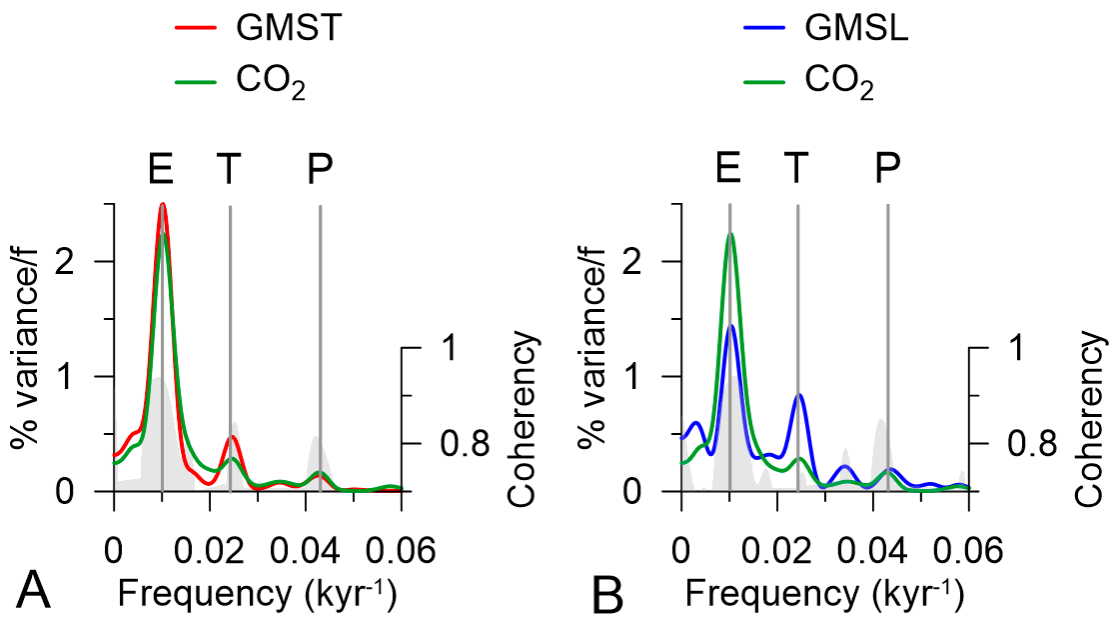

Figure S9. (**A**) Spectral density of global mean surface temperature (GMST) and CO_2 and their coherence spectra (gray shading) for the last 0.8 Myr. (**B**) Spectral density of global mean sea level (GMSL) and CO_2 and their coherence spectra (gray shading) for the last 0.8 Myr. Frequencies of eccentricity (E = 96 kyr), obliquity (T = 41 kyr), and precession (P = 23 kyr) shown by vertical gray lines.

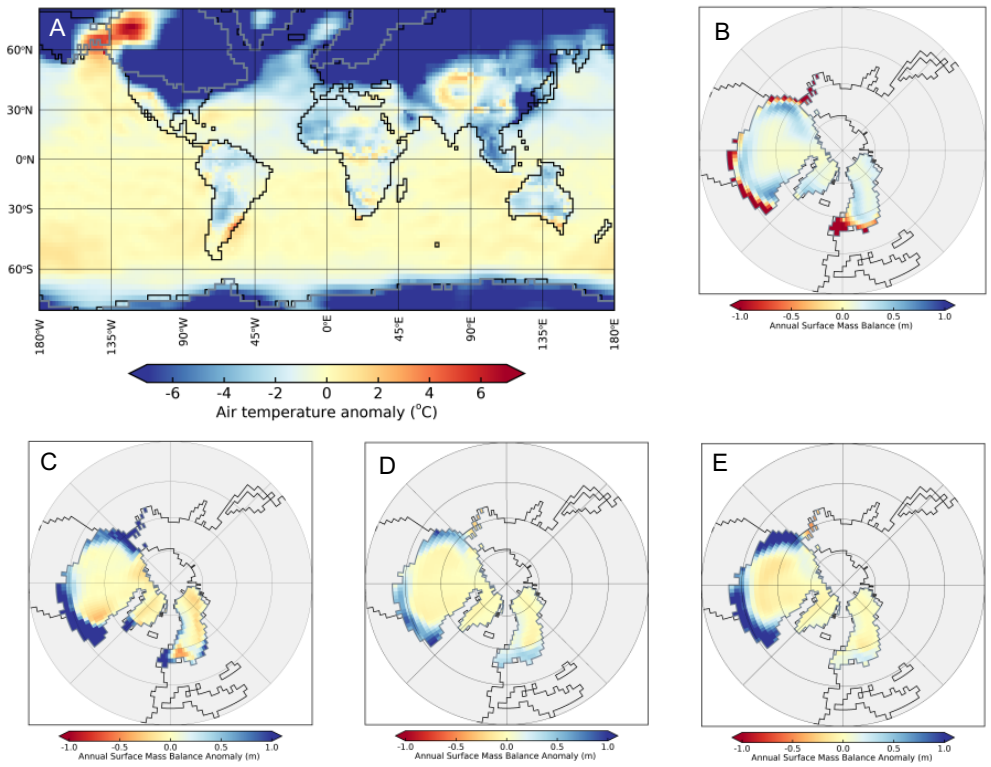

Figure S10. Climate and surface mass balance simulations (Table S1). (**A**) EXP1 minus PI temperature. (**B**) Annual surface mass balance for EXP1. (**C**) EXP2 minus EXP3 annual surface mass balance. (**D**) EXP2 minus EXP5 annual surface mass balance. (**E**) EXP4 minus EXP6 annual surface mass balance. The boundary conditions for the experiments are described in Table S1.

Table S1. Boundary conditions, simulated mean-annual global and Northern Hemisphere temperatures, and ice-sheet mass balances for the North American (NA) and Eurasian (EU) ice-sheet complexes from sensitivity tests conducted with the GENESIS climate model using the 50-meter mixed layer ocean model. MAT is 2-m air temperature.

Experiment	Orbitals[1]	CO_2 (ppmV)	NH ice sheets[2]	Global MAT (K)	Global SST (K)	NH MAT[3] (K)	NH SST[3] (K)	NA SMB (m a^{-1})	EU SMB (m a^{-1})
PI	Present	280	Present	285	288	270	273	--	--
EXP1	LGM	200	GLAC	282	287	261	268	8	0
EXP2	Glacial	300	HIGH	283	288	262	270	5	-6
EXP3	Interglacial	300	HIGH	283	288	263	271	-11	-8
EXP4	Glacial	200	HIGH	281	286	260	268	20	2
EXP5	Glacial	300	GLAC	283	288	262	270	-30	-17
EXP6	Glacial	200	LOW	282	287	261	268	-64	-2

[1]Glacial: 2.165 Ma; Interglacial: 2.145 Ma. Calculated from *Laskar et al.* (*40*).

[2]HIGH: GLAC 1-D LGM ice height with 30 m of additional sea level distributed as 20 m over the LIS and 10 m over the EIS; LOW: GLAC 1-D LGM ice height reduced to 60% of the LGM sea level.

[3]Poleward of 40°N.

Data S1. (separate file)

Data_S1.xlxs file contains global mean sea level data plotted in Fig. 1.

REFERENCES AND NOTES

1. C. Waelbroeck *et al.*, Sea-level and deep water temperature changes derived from benthic foraminifera isotopic records. *Quaternary Science Reviews* **21**, 295-305 (2002).
2. M. Siddall, B. Honisch, C. Waelbroeck, P. Huybers, Changes in deep Pacific temperature during the mid-Pleistocene transition and Quaternary. *Quaternary Science Reviews* **29**, 170-181 (2010).
3. S. L. Bates, M. Siddall, C. Waelbroeck, Hydrographic variations in deep ocean temperature over the mid-Pleistocene transition. *Quaternary Science Reviews* **88**, 147-158 (2014).
4. E. J. Rohling *et al.*, Sea level and deep-sea temperature reconstructions suggest quasi-stable states and critical transitions over the past 40 million years. *Science Advances* **7**, eabf5326 (2021).
5. E. J. Rohling *et al.*, Comparison and synthesis of sea-level and deep-sea temperature variations over the past 40 million years. *Reviews of Geophysics* **60**, e2022RG000775 (2022).
6. R. M. Spratt, L. E. Lisiecki, A Late Pleistocene sea level stack. *Climate of the Past* **12**, 1079-1092 (2016).
7. J. Hansen, M. Sato, G. Russell, P. Kharecha, Climate sensitivity, sea level and atmospheric carbon dioxide. *Philosophical Transactions of the Royal Society A-Mathematical Physical and Engineering Sciences* **371**, 10.1098/rsta.2012.0294 (2013).
8. J. E. Hansen *et al.*, Global warming in the pipeline. *Oxford Open Climate Change* **3**, kgad008 (2023).
9. P. U. Clark *et al.*, Mean ocean temperature change and decomposition of the benthic $d^{18}O$ record over the last 4.5 Myr. *Climate of the Past*, (in review).
10. J. D. Shakun, D. W. Lea, L. E. Lisiecki, M. E. Raymo, An 800-kyr record of global surface ocean delta O-18 and implications for ice volume-temperature coupling. *Earth and Planetary Science Letters* **426**, 58-68 (2015).
11. S. Sosdian, Y. Rosenthal, Deep-sea temperature and ice volume changes across the Pliocene-Pleistocene climate transitions. *Science* **325**, 306-310 (2009).
12. H. Elderfield *et al.*, Evolution of ocean temperature and ice volume through the mid-Pleistocene climate transition. *Science* **337**, 704-709 (2012).
13. S. C. Woodard *et al.*, Antarctic role in Northern Hemisphere glaciation. *Science* **346**, 847-851 (2014).
14. H. L. Ford, M. E. Raymo, Regional and global signals in seawater $\delta^{18}O$ records across the mid-Pleistocene transition. *Geology* **48**, 113-117 (2020).
15. K. G. Miller *et al.*, Cenozoic sea-level and cryospheric evolution from deep-sea geochemical and continental margin records. *Science Advances* **6**, (2020).
16. M. J. Winnick, J. K. Caves, Oxygen isotope mass-balance constraints on Pliocene sea level and East Antarctic Ice Sheet stability. *Geology* **43**, 879-882 (2015).
17. G. S. Dwyer, M. A. Chandler, Mid-Pliocene sea level and continental ice volume based on coupled benthic Mg/Ca palaeotemperatures and oxygen isotopes. *Philosophical Transactions of the Royal Society A-Mathematical Physical and Engineering Sciences* **367**, 157-168 (2009).
18. K. A. Jakob *et al.*, A new sea-level record for the Neogene/Quaternary boundary reveals transition to a more stable East Antarctic Ice Sheet. *Proceedings of the National Academy of Sciences of the United States of America* **117**, 30980-30987 (2020).

19. A. C. Mix, W. F. Ruddiman, Oxygen-isotope analyses and Pleistocene ice volumes. *Quaternary Research* **21**, 1-20 (1984).
20. G. R. Grant *et al.*, Reduced magnitude of Early Pleistocene intensification of Northern Hemisphere Glaciation. *Quaternary Science Reviews* **349**, (2025).
21. G. R. Grant *et al.*, The amplitude and origin of sea-level variability during the Pliocene epoch. *Nature* **574**, 237-241 (2019).
22. E. Gasson, R. M. DeConto, D. Pollard, Modeling the oxygen isotope composition of the Antarctic ice sheet and its significance to Pliocene sea level. *Geology* **44**, 827-830 (2016).
23. D. P. Schrag *et al.*, The oxygen isotopic composition of seawater during the Last Glacial Maximum. *Quaternary Science Reviews* **21**, 331-342 (2002).
24. K. Lambeck, H. Rouby, A. Purcell, Y. Sun, M. Sambridge, Sea level and global ice volumes from the Last Glacial Maximum to the Holocene. *Proceedings of the National Academy of Sciences* **111**, 15296-15303 (2014).
25. N. Lhomme, G. K. C. Clarke, C. Ritz, Global budget of water isotopes inferred from polar ice sheets. *Geophysical Research Letters* **32**, (2005).
26. A. Sima, A. Paul, M. Schulz, J. Oerlemans, Modeling the oxygen-isotopic composition of the North American Ice Sheet and its effect on the isotopic composition of the ocean during the last glacial cycle. *Geophysical Research Letters* **33**, (2006).
27. T. Tharammal, A. Paul, U. Merkel, D. Noone, Influence of Last Glacial Maximum boundary conditions on the global water isotope distribution in an atmospheric general circulation model. *Climate of the Past* **9**, 789-809 (2013).
28. P. U. Clark, J. D. Shakun, Y. Rosenthal, P. Köhler, P. J. Bartlein, Global and regional temperature change over the last 4.5 million years. *Science* **383**, 884-890 (2024).
29. R. M. DeConto, D. Pollard, Contribution of Antarctica to past and future sea-level rise. *Nature* **531**, 591-597 (2016).
30. W. R. Peltier, D. F. Argus, R. Drummond, Space geodesy constrains ice age terminal deglaciation: The global ICE-6G_C (VM5a) model. *Journal of Geophysical Research-Solid Earth* **120**, 450-487 (2015).
31. M. B. Priestley, Evolutionary spectra and non-stationary processes. *Journal of the Royal Statistical Society, Series B* **27**, 204-237 (1965).
32. S. R. Meyers. (https://cran.r-project.org/package=astrochron, 2014).
33. R. C. Team, in *R Foundation for Statistical Computing*. (Vienna, Austria, 2022).
34. D. J. Thomson, Spectrum estimation and harmonic analysis. *Proceedings of the IEEE* **70**, 1055-1096 (1982).
35. S. Developers. (2013).
36. P. Howell, N. Pisias, J. Ballance, J. Baughman, L. Ochs, ARAND Time-Series Analysis Software. (2006).
37. D. Pollard, S. L. Thompson, Climate and ice-sheet mass balance at the Last Glacial Maximum from GENESIS version 2 global climate model. *Quaternary Science Reviews* **16**, 841-863 (1997).
38. S. L. Thompson, D. Pollard, Greenland and Antarctic mass balances for present and doubled atmospheric CO2 from the GENESIS version-2 global climate model. *Journal of Climate* **10**, 871-900 (1997).
39. I. Janssens, P. Huybrechts, The Treatment of Meltwater Retardation in Mass-Balance Parameterizations of the Greenland Ice Sheet. *Annals of Glaciology* **31**, 133-140 (2000).

40. J. Laskar *et al.*, A long term numerical solution for the insolation quantities of the Earth. *Astronomy and Astrophysics* **428**, 261-285 (2004).
41. B. Honisch, N. G. Hemming, D. Archer, M. Siddall, J. F. McManus, Atmospheric Carbon Dioxide Concentration Across the Mid-Pleistocene Transition. *Science* **324**, 1551-1554 (2009).
42. K. A. Dyez, B. Honisch, G. A. Schmidt, Early Pleistocene Obliquity-Scale pCO(2) Variability at similar to 1.5 Million Years Ago. *Paleoceanography and Paleoclimatology* **33**, 1270-1291 (2018).
43. G. Bartoli, B. Honisch, R. E. Zeebe, Atmospheric CO2 decline during the Pliocene intensification of Northern Hemisphere glaciations. *Paleoceanography* **26**, (2011).
44. L. Tarasov, A. S. Dyke, R. M. Neal, W. R. Peltier, A data-calibrated distribution of deglacial chronologies for the North American ice complex from glaciological modeling. *Earth and Planetary Science Letters* **315**, 30-40 (2012).
45. P. U. Clark, D. Pollard, Origin of the middle Pleistocene transition by ice sheet erosion of regolith. *Paleoceanography* **13**, 1-9 (1998).
46. S. Ahn, D. Khider, L. E. Lisiecki, C. E. Lawrence, A probabilistic Pliocene–Pleistocene stack of benthic $\delta^{18}O$ using a profile hidden Markov model. *Dynamics and Statistics of the Climate System* **2**, 1-16 (2017).
47. K. G. Miller *et al.*, High tide of the warm Pliocene: Implications of global sea level for Antarctic deglaciation. *Geology* **40**, 407-410 (2012).
48. O. A. Dumitru *et al.*, Constraints on global mean sea level during Pliocene warmth. *Nature* **574**, 233-236 (2019).
49. F. D. Richards *et al.*, Geodynamically corrected Pliocene shoreline elevations in Australia consistent with midrange projections of Antarctic ice loss. *Science Advances* **9**, (2023).
50. O. A. Dumitru *et al.*, Sea-level stands from the Western Mediterranean over the past 6.5 million years. *Sci Rep-Uk* **11**, 6681 (2021).
51. A. Dutton, J. M. Webster, D. Zwartz, K. Lambeck, B. Wohlfarth, Tropical tales of polar ice: evidence of Last Interglacial polar ice sheet retreat recorded by fossil reefs of the granitic Seychelles islands. *Quaternary Science Reviews* **107**, 182-196 (2015).
52. K. M. Grant *et al.*, Sea-level variability over five glacial cycles. *Nature Communications* **5**, (2014).
53. Y. Yokoyama *et al.*, Rapid glaciation and a two-step sea level plunge into the Last Glacial Maximum. *Nature* **559**, 603-+ (2018).